Supporting Information

Development of NIR Emissive Fully-Fused Bisboron Complexes with π-Conjugated Systems Including Multiple Azo Groups

Masashi Nakamura[1], Masayuki Gon[1], Shin-ichiro Natsuda[1], Yasunari Tamai[1,2], Hideo Ohkita[1], Kazuo Tanaka[1,*], and Yoshiki Chujo[1]

[1]*Department of Polymer Chemistry, Graduate School of Engineering, Kyoto University, Nishikyo-ku, Katsura, Kyoto 615-8510, Japan.*

[2]*Japan Science and Technology Agency (JST), PRESTO, 4-1-8 Honcho Kawaguchi, Saitama 332-0012, Japan*

E-mail: tanaka@poly.synchem.kyoto-u.ac.jp

Contents Page

General

^{1}H, ^{13}C, and ^{11}B spectra were recorded on a JEOL AL400 instrument at 400, 100, and 128 MHz, respectively. Samples were analyzed in $CDCl_3$ and CD_2Cl_2. The chemical shift values were expressed relative to Me_4Si for ^{1}H and ^{13}C NMR as an internal standard in $CDCl_3$ and BF_3•Et_2O for ^{11}B NMR as a capillary standard. Analytical thin layer chromatography (TLC) was performed with silica gel 60 Merck F254 plates. Column chromatography was performed with Wakogel® C-300 silica gel. Recyclable preparative high-performance liquid chromatography (HPLC) was carried out on SHIMADZU LC-20AP using CHIRAL ART Amylose-SA S 5-μm (YMC CO., LTD.) and on Japan Analytical Industry Model LaboACE LC-5060 (JAIGEL-2.5H and 3HH columns) using $CHCl_3$ as an eluent. High-resolution mass (HRMS) spectrometry was performed at the Technical Support Office (Department of Synthetic Chemistry and Biological Chemistry, Graduate School of Engineering, Kyoto University), and the HRMS spectra were obtained on a Thermo Fisher Scientific EXACTIVE spectrometer for electrospray ionization (ESI). UV–vis spectra were recorded on a SHIMADZU UV-3600 spectrophotometer, and samples were analyzed at room temperature. Fluorescence emission spectra were measured with a HORIBA JOBIN YVON Fluorolog-3 and Oxford Optistat DN for temperature control. Absolute photoluminescence (PL) quantum efficiency (Φ_{PL}) was recorded on a Hamamatsu Photonics Quantaurus-QY Plus C13534-01. Cyclic voltammetry (CV) was carried out on a BASALS-Electrochemical-Analyzer Model 600D with a glassy carbon working electrode, a Pt counter electrode, an Ag/AgCl reference electrode, and the ferrocene/ferrocenium (Fc/Fc^{+}) external reference at a scan rate of 0.1 V s^{-1}. The PL lifetime measurement was performed on a Horiba FluoroCube spectrofluorometer system; excitation was carried out using UV and visible diode lasers (NanoLED 369 nm). Elemental analyses were performed at the Microanalytical Center of Kyoto University. X-ray crystallographic analysis was carried out by Rigaku R-AXIS RAPID-F graphite-monochromated MoKα radiation diffractometer with imaging plate. A symmetry-related absorption correction was carried out by using the program ABSCOR.[1] The analysis was carried out with direct methods (SHELX-97[2]) using Yadokari-XG.[3] The programs ORTEP3[4] and Mercury-4.2.0 were used to generate the X-ray structural diagram. Femtosecond transient absorption data were collected with a pump and probe femtosecond transient spectroscopy system. This system consists of a regenerative amplified Ti:sapphire laser (Spectra-Physics, Hurricane) and a transient absorption spectrometer (Ultrafast systems, Helios). The amplified Ti:sapphire laser provided 800 nm fundamental pulses at a repetition rate of 1 kHz with an energy of 0.8 mJ and a pulse width of 100 fs (fwhm), which were split into two optical beams with a beam splitter to generate pump and probe pulses. One fundamental beam was converted into white light pulses employed as probe pulses in the wavelength region from 400 to 800 nm. The other fundamental beam was converted into pump pulses at 400 nm with a second harmonic generator (Spectra-Physics, TP-F). The pump pulses were modulated mechanically at a repetition rate of 500 Hz. Temporal evolution of the probe intensity was recorded with a CMOS linear sensor (Ultrafast Systems, SPEC-VIS). Transient absorption spectra and decays were collected over the time range of −5 ps to 3 ns. Typically, 2500

laser shots were averaged at each delay time to obtain a detectable absorbance change as small as ~10^{-4}. In order to cancel out orientation effects on the dynamics, the polarization direction of the linearly polarized probe pulse was set at the magic angle of 54.7 ° with respect to that of the pump pulse. The sample films were encapsulated in a N_2-filled glovebox. Note that the transient absorption spectra and dynamics were highly reproducible even after several measurements. In other words, the laser irradiation had negligible effects on the sample degradation at least under those experimental conditions.

Materials

Commercially available compounds used without purification:

Dimethyl 1,4-cyclohexanedione-2,5-dicarboxylate (**1**)

Phenylhydrazine (Tokyo Chemical Industry Co, Ltd.)

Butylmagnesium chloride (*n*BuMgCl) (Tokyo Chemical Industry Co, Ltd.)

Boron trifluoride diethyl etherate (≥46.5% BF_3 basis) (BF_3•Et_2O) (Sigma–Aldrich Co. LLC.)

Tert-Butyl nitrite (*t*BuONO) (Tokyo Chemical Industry Co, Ltd.)

2-Naphthol (Tokyo Chemical Industry Co, Ltd.)

Methyl anthranilate (**5**) (Tokyo Chemical Industry Co, Ltd.)

2,6-Naphthalenediol (Tokyo Chemical Industry Co, Ltd.)

Commercially available solvents:

AcOH (FUJIFILM Wako Pure Chemical Industries, Ltd.), toluene (deoxidized grade, FUJIFILM Wako Pure Chemical Industries, Ltd.), CH_2Cl_2 (deoxidized grade, FUJIFILM Wako Pure Chemical Industries, Ltd.), and Et_2NH (FUJIFILM Wako Pure Chemical Industries, Ltd.) were used without purification.

THF (Kanto Chemical Co., Inc.) and Et_3N (Kanto Chemical Co., Inc.) were purified by passage through solvent purification columns under N_2 pressure.[5]

Compounds prepared as described in the literatures:

1,4-Benzenedicarboxylic acid, 2,5-diamino-1,4-dimethyl ester (**2**)[6,7]

Synthetic Procedures and Characterization

Synthesis of 2

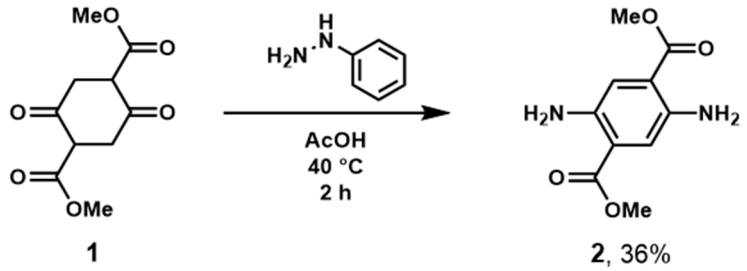

Dimethyl 1,4-cyclohexanedione-2,5-dicarboxylate (**1**) (2.28 g, 10.0 mmol) was dissolved in AcOH (30 mL) in a round-bottom flask equipped with a magnetic stirring bar. Phenylhydrazine (4.87 g, 45.0 mmol) was dropwisely added to the flask. The reaction was carried out at 40 °C for 2 h. After the reaction, H_2O (60 mL) and EtOAc (60 mL) were added to the reaction mixture at room temperature for dilution of the solution, and the organic layer was extracted with EtOAc. The organic layer was washed with brine and dried over Na_2SO_4. Na_2SO_4 was removed by filtration, and the solvent was removed with a rotary evaporator. The residue was semi-purified by column chromatography on SiO_2 (hexane/EtOAc = 7/3 v/v as an eluent). The obtained orange solid was purified by recrystallization with hexane (poor solvent) and EtOAc (good solvent) to afford **2** (0.81 g, 3.61 mmol, 36%) as an orange crystal.

2: R_f = 0.25 (hexane/EtOAc = 7/3 v/v). ^{1}H NMR ($CDCl_3$, 400 MHz) δ 7.28 (s, 2H), 5.07 (bs, 2H), 3.88 (s, 6H) ppm; ^{13}C NMR ($CDCl_3$, 100 MHz) δ 167.6, 140.5, 118.9, 117.5, 51.9 ppm; HRMS (ESI) calcd. for $C_{10}H_{13}N_2O_4Na$ $[M+Na]^+$: 225.0870, found: 225.0872. Elemental analysis calcd. for $C_{10}H_{12}N_2O_4$: C 53.57 H 5.39 N 12.49, found: C 53.36 H 5.47 N 12.48.

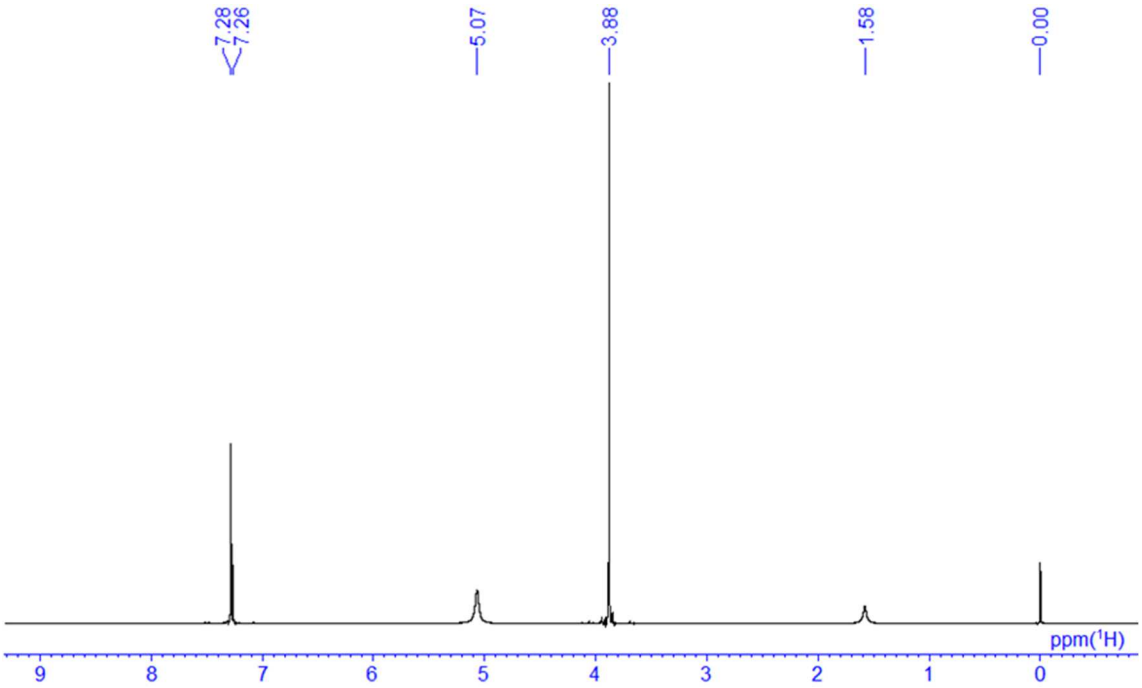

Chart 1. ^{1}H NMR spectrum of **2** in $CDCl_3$.

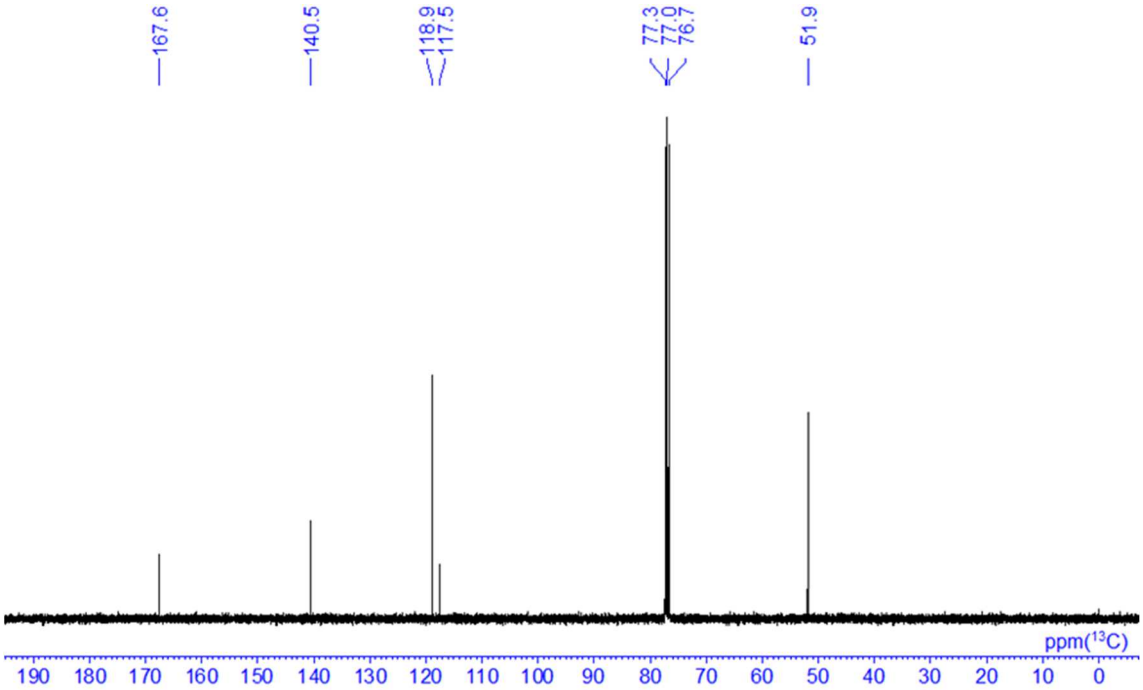

Chart 2. ^{13}C NMR spectrum of **2** in $CDCl_3$.

Synthesis of 3

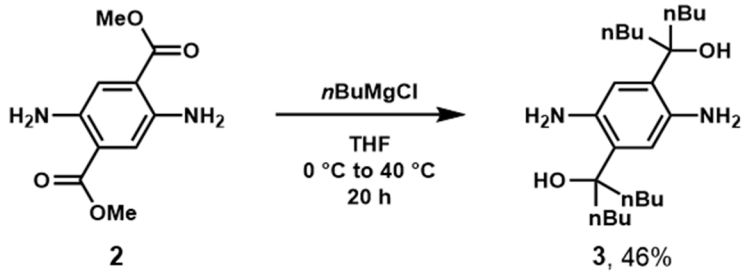

2 (0.99 g, 4.42 mmol) was placed in a round-bottom flask equipped with a magnetic stirring bar. After degassing and filling N_2 three times, THF (15 mL) was added to the flask. After cooling the mixture to 0 °C, *n*-BuMgCl (2 M in THF, 18 mL, 19.9 mmol) was dropwisely added. The reaction was carried out at 40 °C for 20 h. After the reaction, saturated aqueous NH_4Cl was added to the reaction mixture at 0 °C for quenching the reaction, and the organic layer was extracted with EtOAc. The organic layer was washed with brine and dried over Na_2SO_4. Na_2SO_4 was removed by filtration, and the solvent was removed with a rotary evaporator. The residue was purified by recrystallization with hexane (poor solvent) and EtOAc (good solvent) to afford **3** (0.80 g, 2.03 mmol, 46%) as a gray solid.

3: R_f = 0.42 ($CHCl_3$/MeOH = 19/1 v/v). ^{1}H NMR ($CDCl_3$, 400 MHz) δ 6.37 (s, 2H), 3.82 (bs, 4H), 1.91–1.77 (m, 8H), 1.35–1.18 (m, 16H), 0.88 (t, J = 6.8 Hz, 12H) ppm; ^{13}C NMR ($CDCl_3$, 100 MHz) δ 136.8, 130.5, 119.3, 78.7, 40.0, 26.0, 23.2, 14.1 ppm. HRMS (ESI) calcd. for $C_{24}H_{44}N_2O_2Na$ $[M+Na]^+$: 415.3295, found: 415.3297. Elemental analysis calcd. for $C_{24}H_{44}N_2O_2$: C 73.42 H 11.30 N 7.13, found: C 73.21 H 11.37 N 7.04.

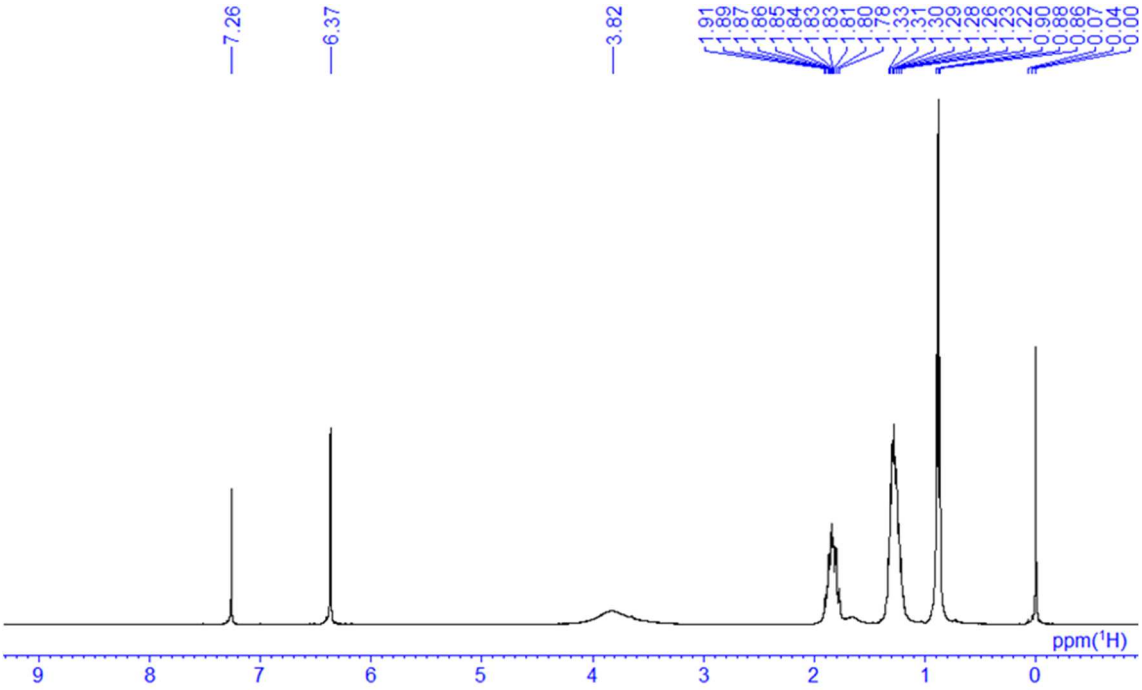

Chart 3. ^{1}H NMR spectrum of **3** in $CDCl_3$.

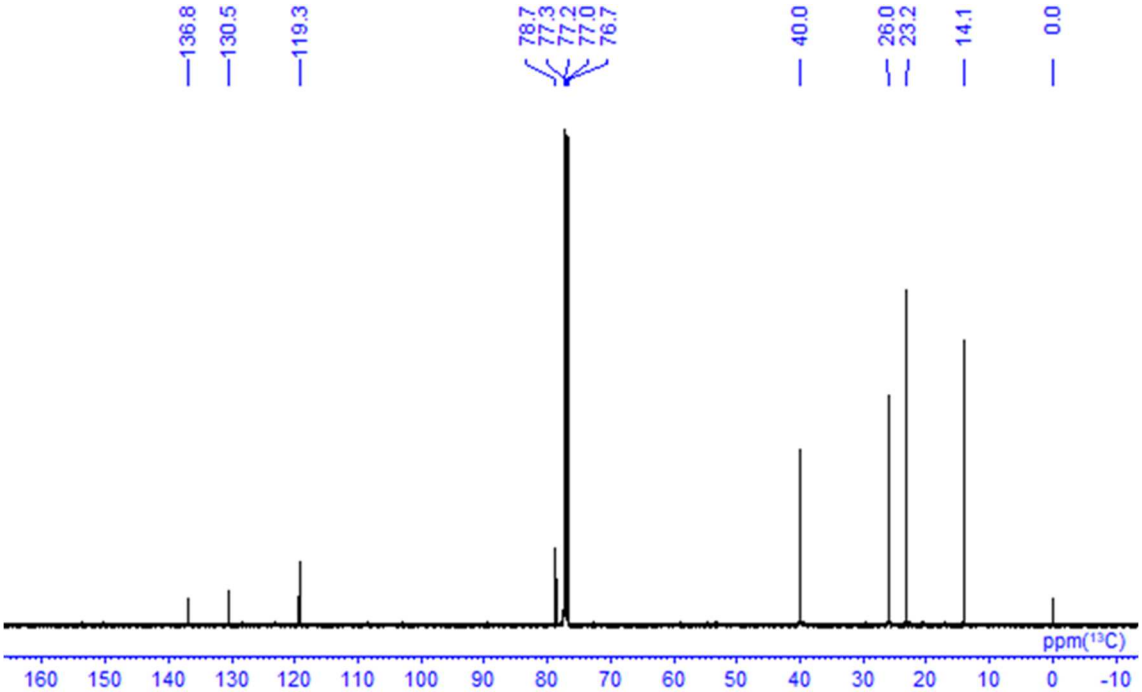

Chart 4. ^{13}C NMR spectrum of **3** in $CDCl_3$.

Synthesis of B2b

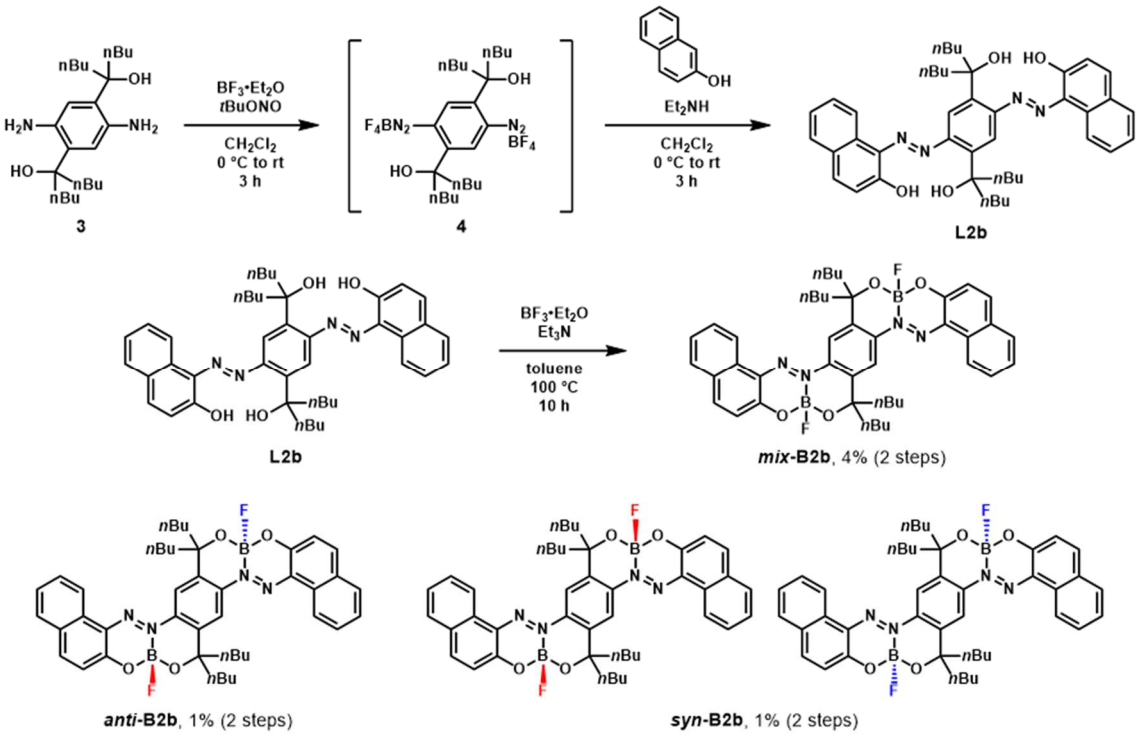

3 (0.53 g, 1.35 mmol) was placed in a round-bottom flask equipped with a magnetic stirring bar. After degassing and filling N_2 three times, CH_2Cl_2 (30 mL) was added to the flask. After cooling the mixture to 0 °C, BF_3•Et_2O (0.51 mL, 4.06 mmol) and *t*BuONO (0.39 mL, 3.25 mmol) were dropwisely added to the mixture. The reaction was carried out at room temperature for 3 h to afford **4** as crude.

2-Naphthol (0.39 g, 2.71 mmol) was dissolved in CH_2Cl_2 (10 mL) in another round-bottom flask equipped with a magnetic stirring bar. **4** was dropwisely added with Pasteur pipette and Et_2NH (0.84 mL, 8.12 mmol) to the flask. The reaction was carried out at room temperature for 3 h. After the reaction, the solvent was removed with a rotary evaporator. The residue was purified by column chromatography on SiO_2 (CH_2Cl_2/EtOAc = 9/1 v/v as an eluent) to afford **L2b** (0.12 g, 0.17 mmol, 13%) as purple powder. The obtained purple powder **L2b** was used for the next reaction without further purification. **L2b** (0.12 g, 0.17 mmol) was placed in a round-bottom flask equipped with a magnetic stirring bar. After degassing and filling N_2 three times, toluene (20 mL) was added to the flask. BF_3•Et_2O (0.21 mL, 1.71 mmol) and Et_3N (0.12 mL, 0.85 mmol) were added to the mixture. After finishing the addition, the reaction was carried out at 100 °C for 10 h. After the reaction, the solvent was removed with a rotary evaporator. The residue was purified by column chromatography on SiO_2 (hexane/CH_2Cl_2 = 1/2 v/v as eluent) to afford ***mix*-B2b** (0.037 g, 0.049 mmol, 4%, 2 steps from **3**) which were a mixture of two diastereomers, ***anti*-B2b** and ***syn*-B2b**, as a dark red powder. ***mix*-B2b** was separated each diastereomer with chiral high performance liquid

chromatography (hexane/THF = 4/1 v/v as an eluent). The first and third peaks were ***syn*-B2b** and the second peak was ***anti*-B2b**. Both fractions were purified with high performance liquid chromatography ($CHCl_3$ as eluent) followed by flash column chromatography ($CHCl_3$ as eluent) to afford ***anti*-B2b** (0.011 g, 0.015 mmol, 1%, 2 steps from **3**) as a dark red powder and ***syn*-B2b** (0.011 g, 0.015 mmol, 1%, 2 steps from **3**) as a dark red powder.

***anti*-B2b**: R_f = 0.22 (CH_2Cl_2/hexane = 2/1 v/v). ^{1}H NMR (CD_2Cl_2, 400 MHz) δ 8.64 (d, J = 7.6 Hz, 2H), 8.24 (s, 2H), 8.17 (d, J = 9.0 Hz, 2H), 7.87 (d, J = 8.0 Hz, 2H), 7.83–7.79 (m, 2H), 7.63–7.59 (m, 2H), 7.26 (d, J = 9.0 Hz, 2H), 2.29–2.22 (m, 2H), 2.14–2.06 (m, 2H), 2.01–1.89 (m, 4H), 1.70–1.62 (m, 4H), 1.49–1.15 (m, 10H), 1.06–0.78 (m, 2H), 1.00 (t, J = 7.3 Hz, 6H), 0.74 (t, J = 7.3 Hz, 6H) ppm; ^{13}C NMR (CD_2Cl_2, 100 MHz) δ 155.5, 144.1, 142.0, 141.6, 133.4, 132.2, 130.8, 129.8, 129.4, 127.1, 121.9, 120.8, 117.5, 79.0, 43.8, 42.9, 26.4, 26.2, 23.6, 23.4, 14.3, 14.2 ppm; ^{11}B NMR (CD_2Cl_2, 128 MHz) δ −0.29 ppm.

***syn*-B2b**: R_f = 0.21 (CH_2Cl_2/hexane = 2/1 v/v). ^{1}H NMR (CD_2Cl_2, 400 MHz) δ 8.65 (d, J = 8.3 Hz, 2H), 8.22 (s, 2H), 8.17 (d, J = 9.2 Hz, 2H), 7.87 (d, J = 8.1 Hz, 2H), 7.83–7.78 (m, 2H), 7.63–7.59 (m, 2H), 7.27 (d, J = 9.0 Hz, 2H), 2.35–2.27 (m, 2H), 2.14–1.97 (m, 4H), 1.92–1.84 (m, 2H), 1.75–1.66 (m, 4H), 1.45–1.22 (m, 10H), 1.07–0.74 (m, 2H), 0.95 (t, J = 7.3 Hz, 6H), 0.83 (t, J = 7.3 Hz, 6H) ppm; ^{13}C NMR (CD_2Cl_2, 100 MHz) δ 155.6, 144.1, 142.0, 141.6, 133.4, 132.3, 130.8, 129.8, 129.4, 127.1, 121.9, 120.8, 117.4, 79.0, 44.0, 42.7, 26.5, 26.1, 23.7, 23.3, 14.3, 14.1 ppm; ^{11}B NMR (CD_2Cl_2, 128 MHz) δ −0.29 ppm.

***mix*-B2b**: HRMS (ESI) calcd. for $C_{44}H_{50}B_2F_2N_4O_4Na$ $[M+Na]^+$: 781.3878, found: 781.3894. Elemental analysis calcd. for $C_{44}H_{50}B_2F_2N_4O_4$: C 69.67 H 6.64 N 7.39, found: C 69.65 H 6.78 N 7.48.

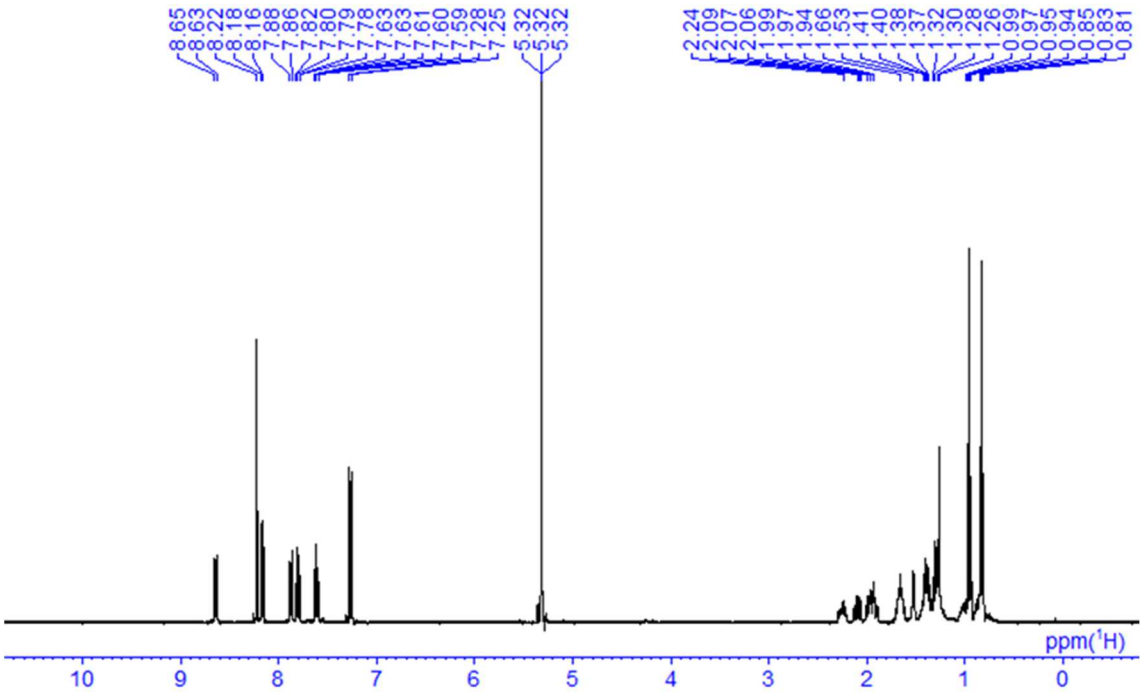

Chart 5. ^{1}H NMR spectrum of ***anti*-B2b** in CD_2Cl_2.

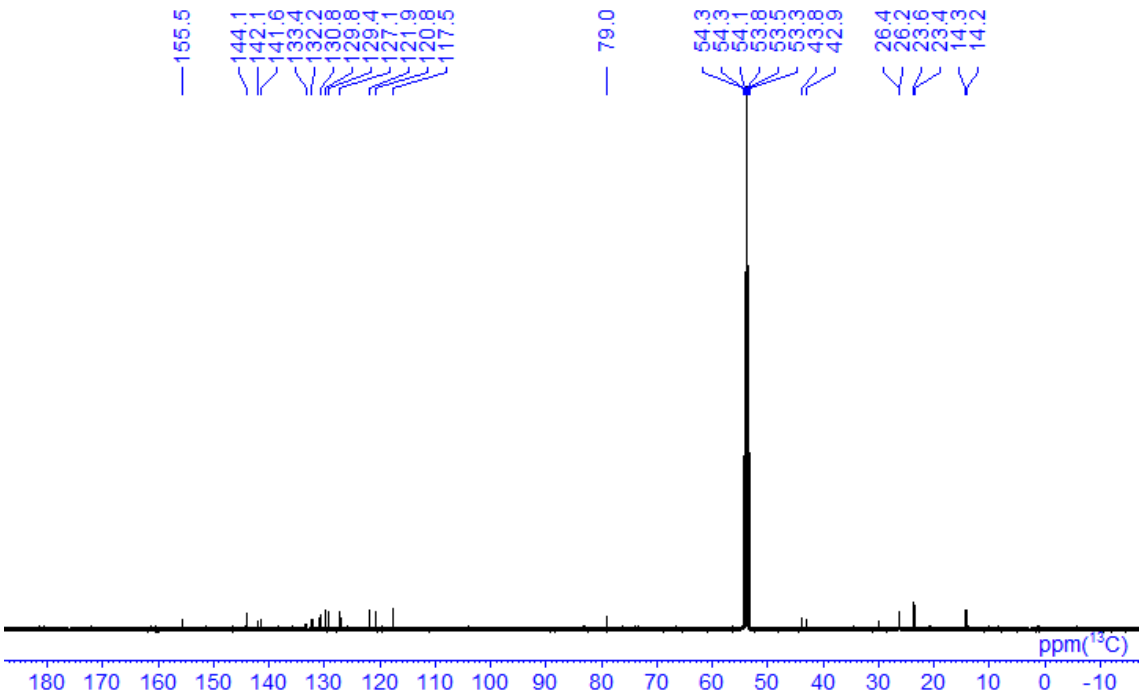

Chart 6. ^{13}C NMR spectrum of ***anti*-B2b** in CD_2Cl_2.

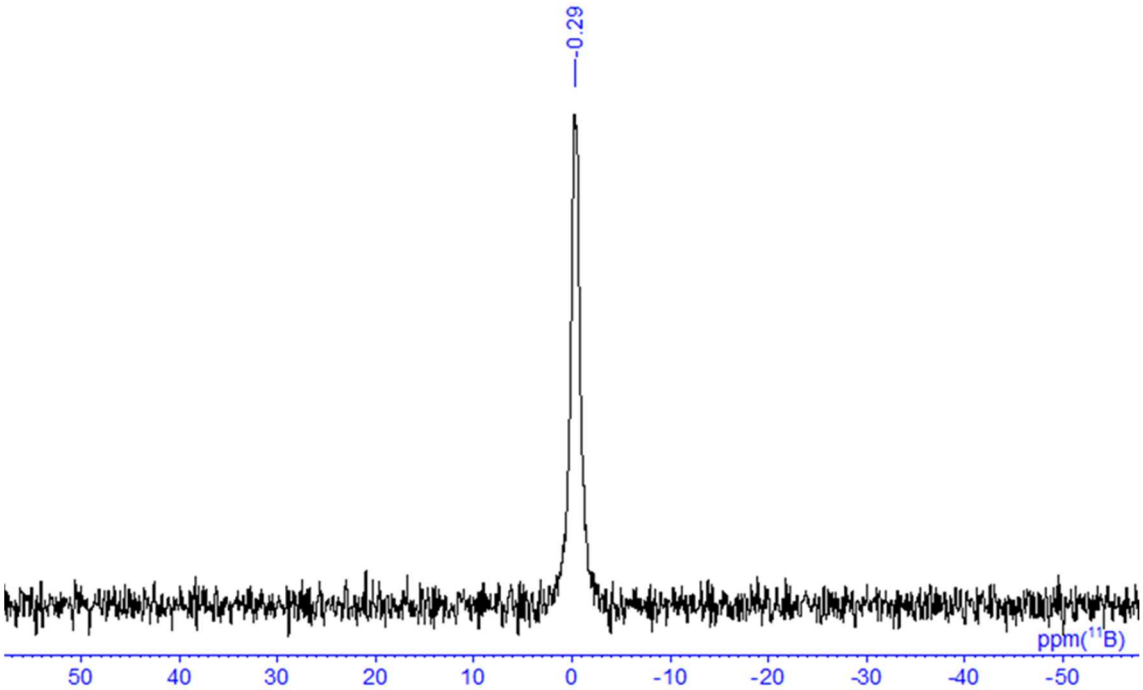

Chart 7. ^{11}B NMR spectrum of ***anti*-B2b** in CD_2Cl_2.

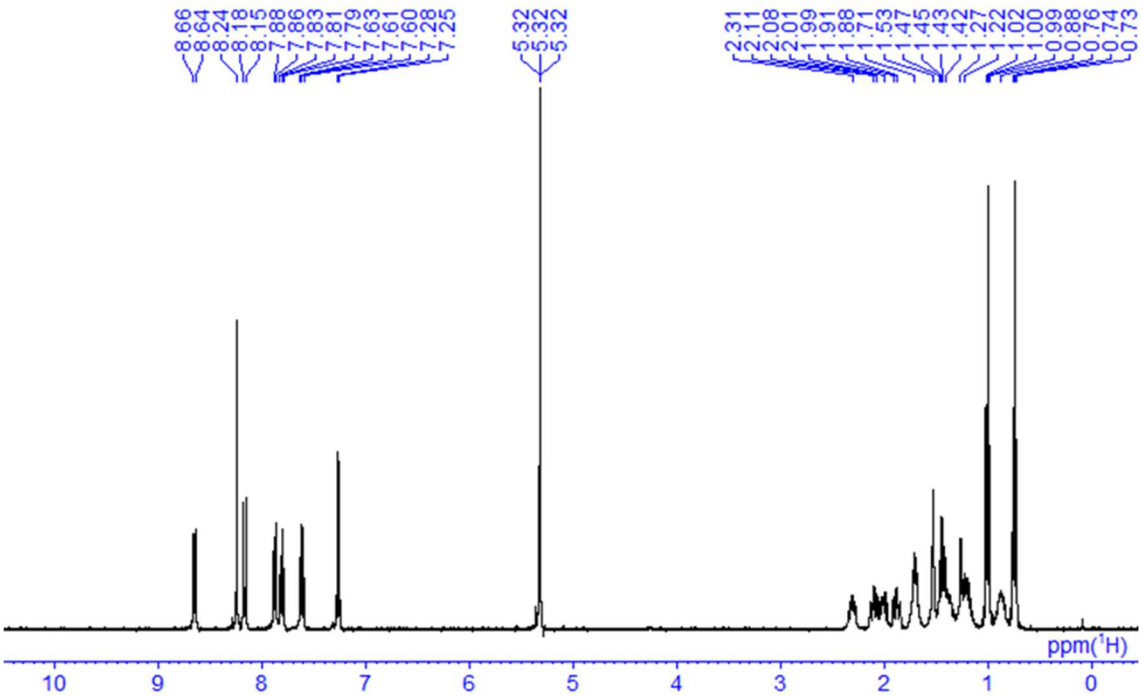

Chart 8. ^{1}H NMR spectrum of ***syn*-B2b** in CD_2Cl_2.

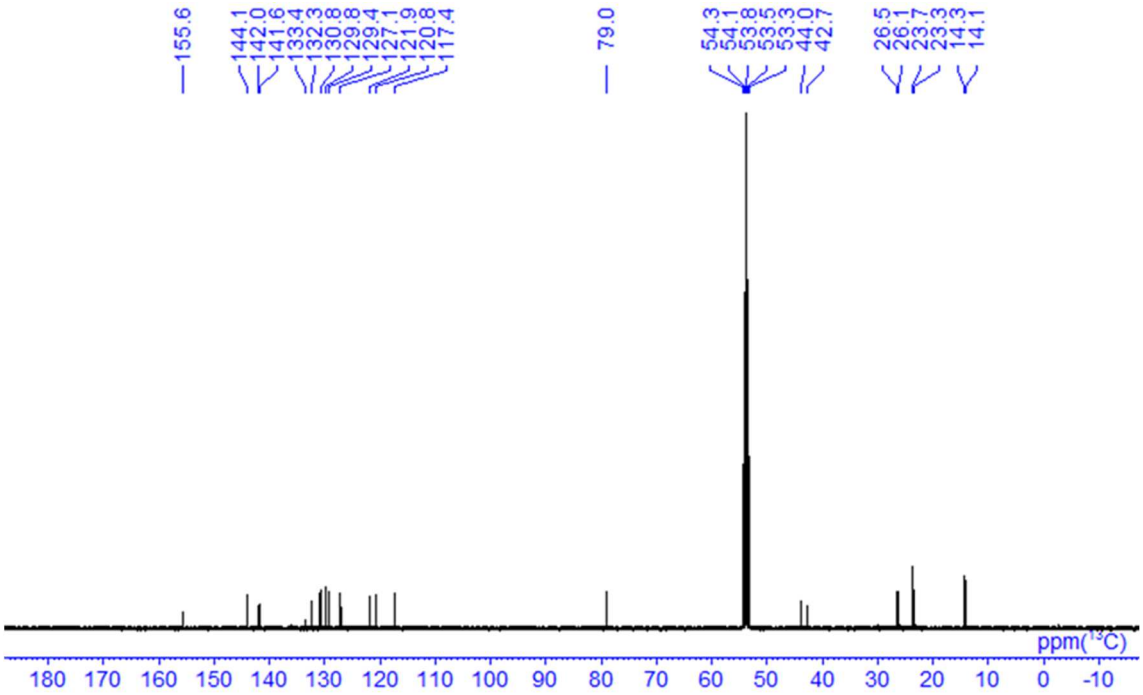

Chart 9. ^{13}C NMR spectrum of ***syn*-B2b** in CD_2Cl_2.

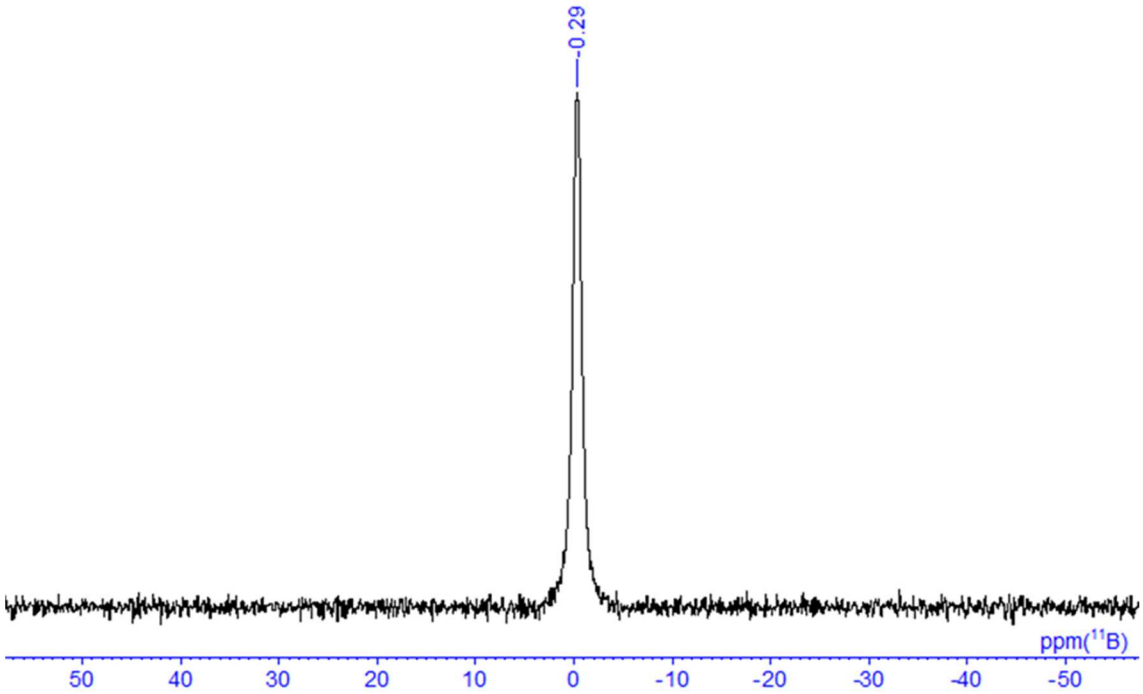

Chart 10. ^{11}B NMR spectrum of ***syn*-B2b** in CD_2Cl_2.

Synthesis of 6

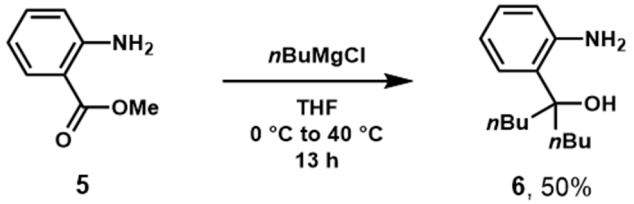

Methyl anthranilate **5** (1.00 g, 6.62 mmol) was placed in a round-bottom flask equipped with a magnetic stirring bar. After degassing and filling N_2 three times, THF (22 mL) was added to the flask. After cooling the mixture to 0 °C, *n*BuMgCl (2 M in THF, 19.9 mL, 19.9 mmol) was dropwisely added. The reaction was carried out at 40 °C for 13 h. After the reaction, saturated aqueous NH_4Cl was added to the reaction mixture at 0 °C for quenching the reaction, and the organic layer was extracted with EtOAc. The organic layer was washed with brine and dried over Na_2SO_4. Na_2SO_4 was removed by filtration, and the solvent was removed with a rotary evaporator. The residue was purified by column chromatography on SiO_2 (CH_2Cl_2/EtOAc = 9/1 v/v as an eluent) to afford **6** (0.78 g, 3.31 mmol, 50%) as a pale-yellow oil.

6: R_f = 0.45 (CH_2Cl_2/EtOAc = 9/1 v/v). ^{1}H NMR ($CDCl_3$, 400 MHz) δ 7.03 (dt, J = 8.2, 0.6 Hz, 1H), 6.96 (dd, J = 7.8, 0.9 Hz, 1H), 6.67 (t, J = 7.7 Hz, 1H), 6.61 (dd, J = 8.0, 1.1 Hz, 1H), 4.67 (bs, 2H), 1.98–1.84 (m, 4H), 1.32-1.15 (m, 8H), 0.88 (t, 6H) ppm; ^{13}C NMR ($CDCl_3$, 100 MHz) δ 146.2, 127.9, 127.8, 127.5, 117.8, 117.3, 79.4, 39.4, 26.0, 23.1, 14.1 ppm. HRMS (ESI) calcd. for $C_{15}H_{25}NONa$ $[M+Na]^+$: 258.1828, found: 258.1830. Elemental analysis calcd. for $C_{15}H_{25}NO$: C 76.55 H 10.71 N 5.95, found: C 76.32 H 10.89 N 5.88.

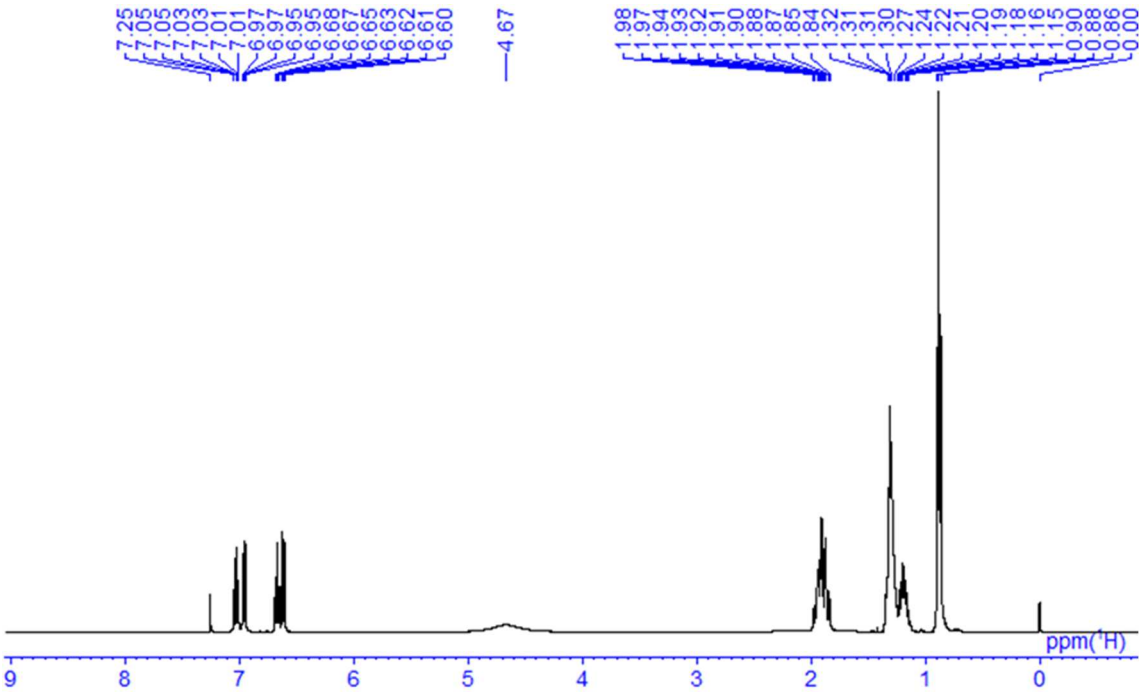

Chart 11. ^{1}H NMR spectrum of **6** in $CDCl_3$.

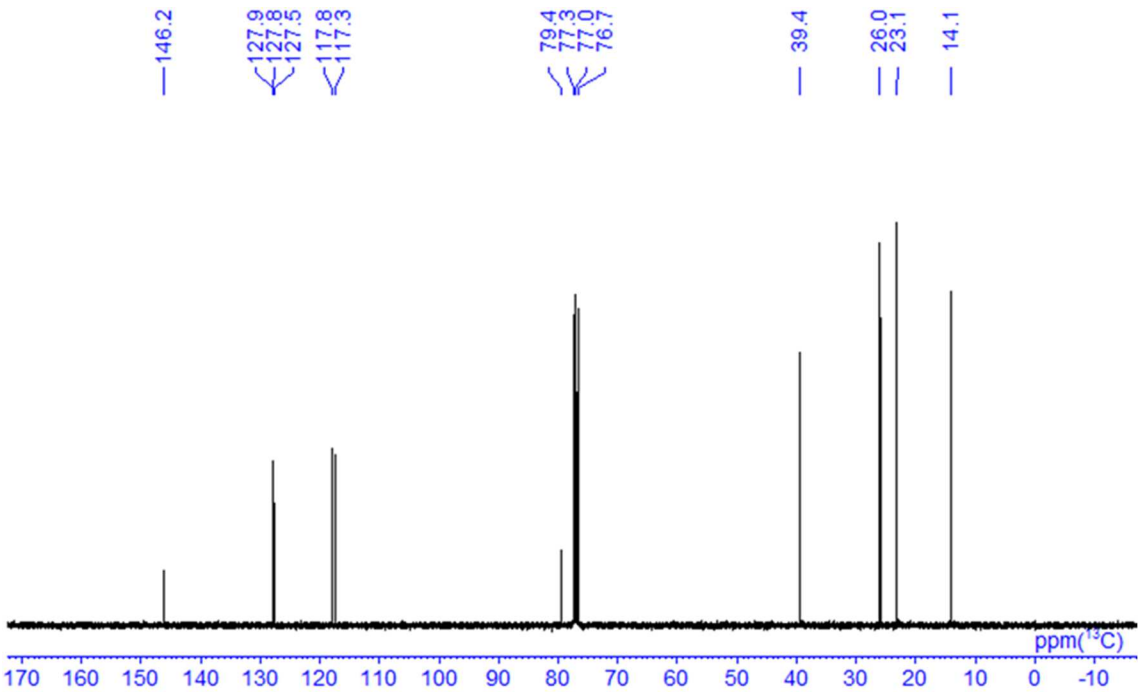

Chart 12. ^{13}C NMR spectrum of **6** in $CDCl_3$.

Synthesis of B1

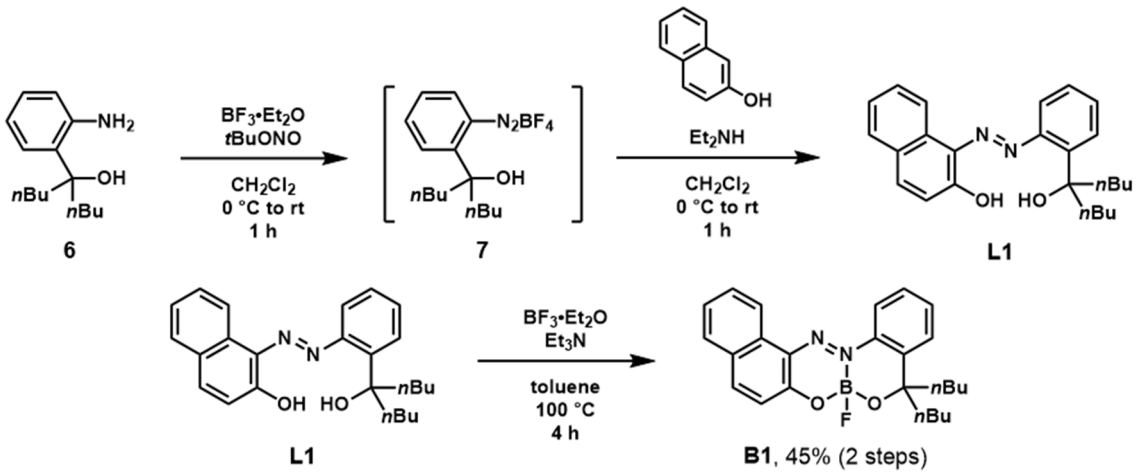

6 (0.26 g, 1.12 mmol) was placed in a round-bottom flask equipped with a magnetic stirring bar. After degassing and filling N_2 three times, CH_2Cl_2 (10 mL) was added to the flask. After cooling the mixture to 0 °C, BF_3•Et_2O (0.21 mL, 1.68 mmol) and *t*BuONO (0.16 mL, 1.34 mmol) were dropwisely added to the mixture. The reaction was carried out at room temperature for 1 h to afford **7** as crude. 2-Naphthol (0.16 g, 1.12 mmol) was dissolved in CH_2Cl_2 (10 mL) in another round-bottom flask equipped with a magnetic stirring bar. **7** was dropwisely added with Pasteur pipette and Et_2NH (0.35 mL, 3.35 mmol) to the flask. The reaction was carried out at room temperature for 1 h. After the reaction, the solvent was removed with a rotary evaporator. The residue was purified by column chromatography on SiO_2 (hexane/EtOAc = 3/1 v/v as an eluent) to afford **L1** (0.38 g, 0.96 mmol, 86%) as red oil. The obtained red oil **L1** was used for the next reaction without further purification. **L1** (0.38 g, 0.96 mmol) was placed in a round-bottom flask equipped with a magnetic stirring bar. After degassing and filling N_2 three times, toluene (10 mL) was added to the flask. BF_3•Et_2O (0.48 mL, 3.85 mmol) and Et_3N (0.27 mL, 1.93 mmol) were added to the mixture. After finishing the addition, the reaction was carried out at 100 °C for 4 h. After the reaction, the solvent was removed with a rotary evaporator. The residue was purified by column chromatography on SiO_2 (hexane/CH_2Cl_2 = 2/3 v/v as an eluent) to afford **B1** (0.20 g, 0.48 mmol, 43%, 2 steps from **6**) as a red solid.

B1: R_f = 0.36 (CH_2Cl_2/hexane = 2/1 v/v). ^{1}H NMR (CD_2Cl_2, 400 MHz) δ 8.68 (dd, J = 8.4, 0.6 Hz, 1H), 8.35 (dd, J = 8.1, 1.5 Hz, 1H), 8.10 (d, J = 9.1 Hz, 1H), 7.84 (d, J = 8.0 Hz, 1H), 7.57–7.44 (m, 3H), 7,31 (dd, J = 7.8, 1.5 Hz, 1H), 7.24 (d, J = 9.1 Hz, 1H), 2.20–2.13 (m, 1H), 2.02–1.95 (m, 1H), 1.89–1.73 (m, 2H), 1.63–1.53 (m, 3H), 1.39–1.13 (m, 5H), 0.93 (t, J = 7.3 Hz, 3H), 0.75 (t, J = 7.3 Hz, 3H) ppm; ^{13}C NMR (CD_2Cl_2, 100 MHz) δ 154.1, 142.4, 142.2, 140.7, 132.4, 132.2, 131.6, 130.3, 129.4, 129.2, 128.3, 128.0, 126.6, 121.7, 120.7, 118.8, 79.1, 43.9, 43.0, 26.4, 26.1, 23.7, 23.4, 14.3, 14.2 ppm; ^{11}B NMR (CD_2Cl_2,

128 MHz) δ −0.20 (d, J = 24 Hz) ppm. HRMS (ESI) calcd. for $C_{25}H_{28}BFN_2O_2Na$ $[M+Na]^+$: 441.2120, found: 441.2118. Elemental analysis calcd. for $C_{25}H_{28}BFN_2O_2$: C 71.78 H 6.75 N 6.70, found: C 71.67 H 6.87 N 6.74.

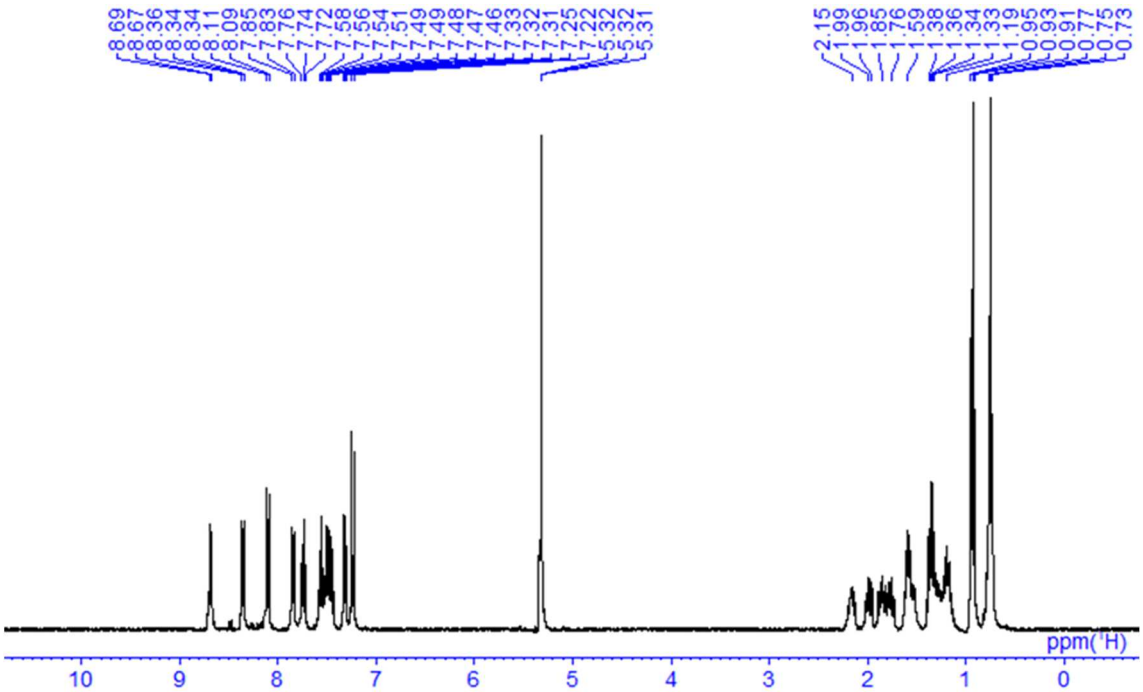

Chart 13. ^{1}H NMR spectrum of **B1** in CD_2Cl_2.

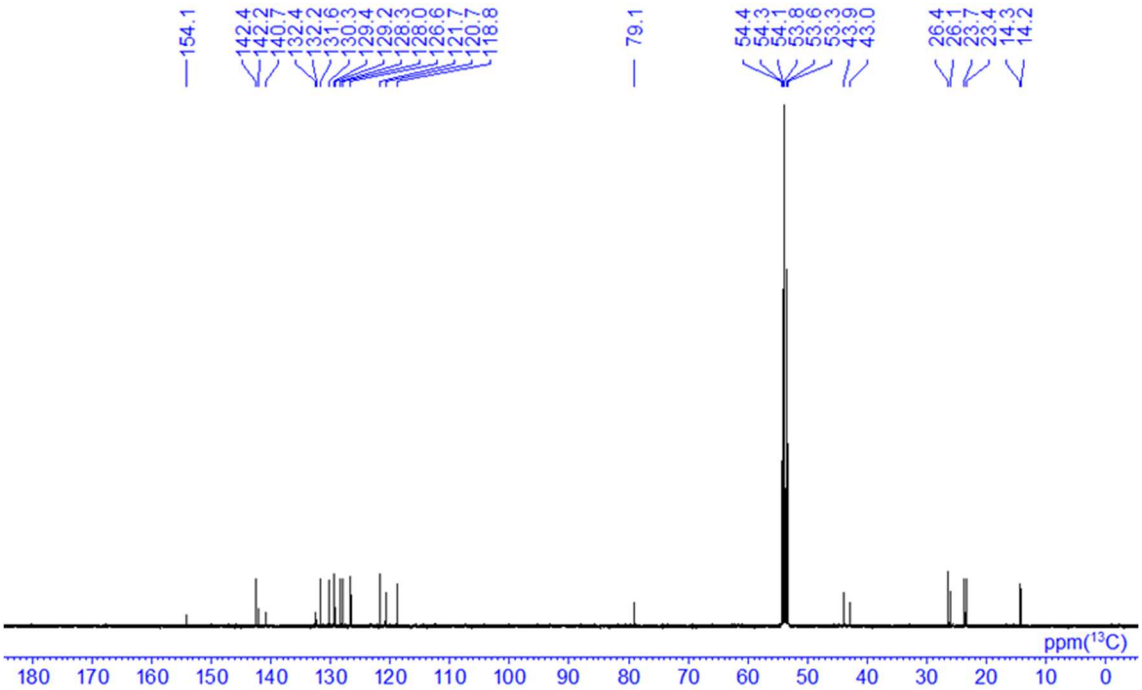

Chart 14. ^{13}C NMR spectrum of **B1** in CD_2Cl_2.

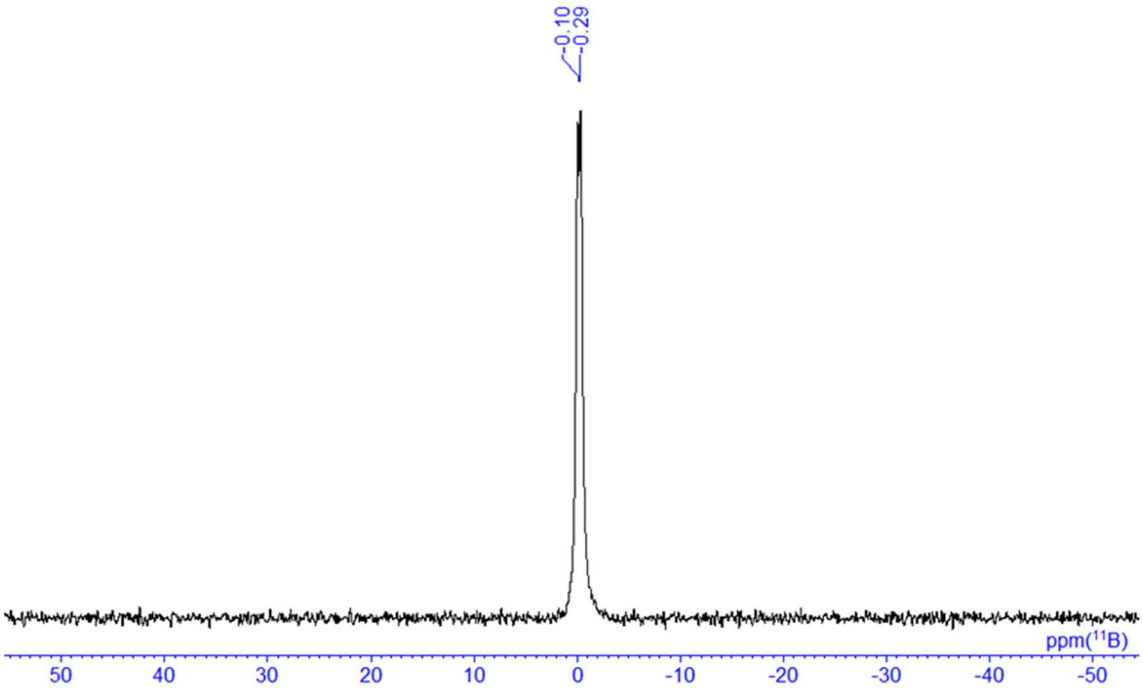

Chart 15. ^{11}B NMR spectrum of **B1** in CD_2Cl_2.

Synthesis of B2n

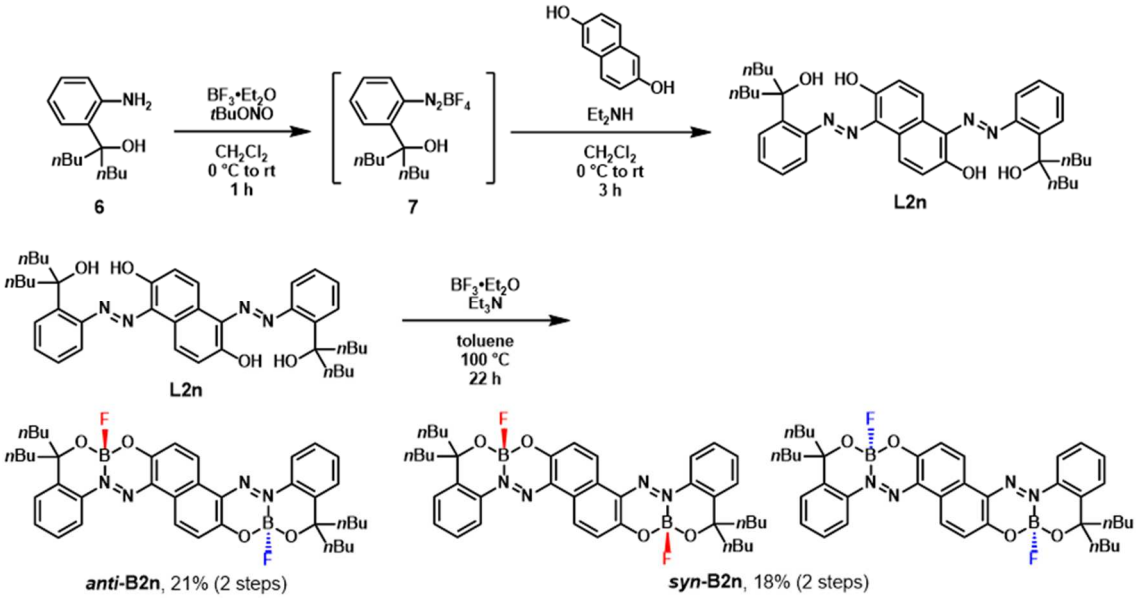

6 (0.41 g, 1.73 mmol) was placed in a round-bottom flask equipped with a magnetic stirring bar. After degassing and filling N_2 three times, CH_2Cl_2 (20 mL) was added to the flask. After cooling the mixture to 0 °C, BF_3•Et_2O (0.31 mL, 2.48 mmol) and *t*BuONO (0.24 mL, 2.07 mmol) were dropwisely added to the mixture. The reaction was carried out at room temperature for 1 h to afford **7** as crude. 2,6-Naphthalenediol (**10**) (0.13 g, 0.83 mmol) was dissolved in CH_2Cl_2 (5 mL) in another round-bottom flask equipped with a magnetic stirring bar. **7** was dropwisely added with Pasteur pipette and Et_2NH (0.51 mL, 4.96 mmol) to the flask. The reaction was carried out at room temperature for 3 h. After the reaction, the solvent was removed with a rotary evaporator. The residue was purified by column chromatography on SiO_2 (CH_2Cl_2/EtOAc = 9/1 v/v as an eluent) to afford **L2n** (0.20 g, 0.31 mmol, 37%) as a dark purple powder. The obtained dark purple powder **L2n** was used for the next reaction without further purification. **L2n** (0.20 g, 0.31 mmol) was placed in a round-bottom flask equipped with a magnetic stirring bar. After degassing and filling N_2 three times, toluene (40 mL) was added to the flask. BF_3•Et_2O (0.38 mL, 3.06 mmol) and Et_3N (0.21 mL, 1.53 mmol) were added to the mixture. After finishing the addition, the reaction was carried out at 100 °C for 22 h. After the reaction, the solvent was removed with a rotary evaporator. The residue was purified by column chromatography on SiO_2 (CH2Cl2/hexane = 2/1 v/v as an eluent) to afford ***anti*-B2n** (0.045 g, 0.064 mmol, 21%, 3 steps from **6**) as a red powder and ***syn*-B2n** (0.040 g, 0.056 mmol, 18%, 3 steps from **6**) as a red solid.

***anti*-B2n**: R_f = 0.29 (CH_2Cl_2/hexane = 2/1 v/v). ^{1}H NMR ($CDCl_3$, 400 MHz) δ 8.96 (d, J = 9.1 Hz, 2H), 8.34 (dd, J = 8.4, 1.2 Hz, 2H), 7.57 (dt, J = 7.8, 1.3 Hz, 2H) 7.50–7.46 (m, 4H), 7,35 (dd, J = 8.0, 1.2

Hz, 2H), 2.23–2.15 (m, 2H), 2.06–1.99 (m, 2H), 1.91–1.75 (m, 4H), 1.64–1.57 (m, 2H), 1.41–1.15 (m, 6H), 0.94 (t, J = 7.2 Hz, 3H), 0.76 (t, J = 7.3 Hz, 3H) ppm; ^{13}C NMR (CD_2Cl_2, 100 MHz) δ 152.5, 143.1, 143.1, 140.6, 134.5, 134.4, 132.6, 132.6, 128.4, 128.4, 128.1, 127.4, 127.3, 123.7, 123.6, 119.1, 79.2, 43.9, 42.9, 26.4, 26.1, 23.6, 23.3, 14.3, 14.2 ppm; ^{11}B NMR (CD_2Cl_2, 128 MHz) δ −0.10 ppm. HRMS (ESI) calcd. for $C_{40}H_{48}B_2F_2N_4O_4$ [M•]$^-$: 708.3835, found: 708.3840. Elemental analysis calcd. for $C_{40}H_{48}B_2F_2N_4O_4$: C 67.81 H 6.83 N 7.91, found: C 67.54 H 6.93 N 7.83.

***syn*-B2n**: R_f = 0.19 (CH_2Cl_2/hexane = 2/1 v/v). ^{1}H NMR (CD_2Cl_2, 400 MHz) δ 8.97 (d, J = 9.0 Hz, 2H), 8.32 (dd, J = 8.6, 1.0 Hz, 2H), 7.55 (dt, J = 7.3, 1.0 Hz, 2H) 7.48–7.42 (m, 4H), 7,34 (dd, J = 7.8, 1.2 Hz, 2H), 2.24–2.17 (m, 2H), 2.06–1.99 (m, 2H), 1.92–1.74 (m, 4H), 1.65–1.58 (m, 2H), 1.42–1.11 (m, 6H), 0.95 (t, J = 7.3 Hz, 3H), 0.75 (t, J = 7.3 Hz, 3H) ppm; ^{13}C NMR (CD_2Cl_2, 100 MHz) δ 152.5, 143.1, 143.1, 140.7, 134.5, 134.4, 132.6, 132.1, 128.4, 128.4, 128.1, 128.1, 127.3, 123.7, 123.7, 119.1, 79.3, 43.9, 42.9, 26.4, 26.1, 23.7, 23.3, 14.3, 14.2 ppm; ^{11}B NMR (CD_2Cl_2, 128 MHz) δ −0.10 ppm. HRMS (ESI) calcd. for $C_{40}H_{48}B_2F_2N_4O_4$ [M•]$^-$: 708.3835, found: 708.3846. Elemental analysis calcd. for $C_{40}H_{48}B_2F_2N_4O_4$: C 67.81 H 6.83 N 7.91, found: C 67.72 H 6.87 N 7.70.

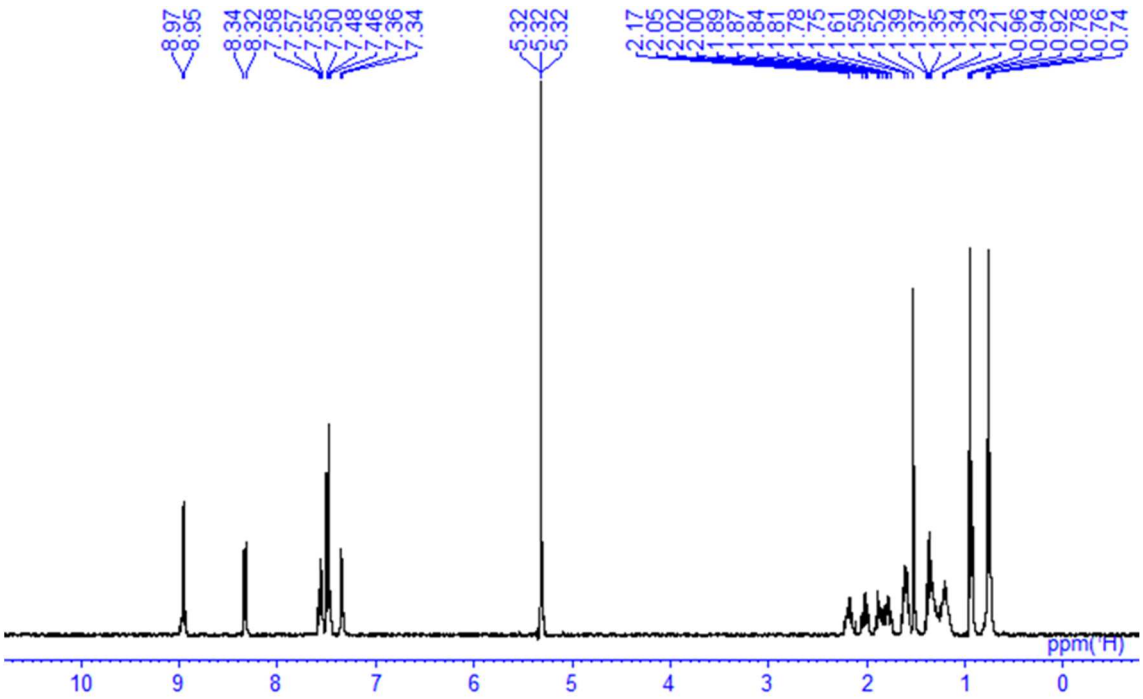

Chart 16. ^{1}H NMR spectrum of ***anti*-B2n** in CD_2Cl_2.

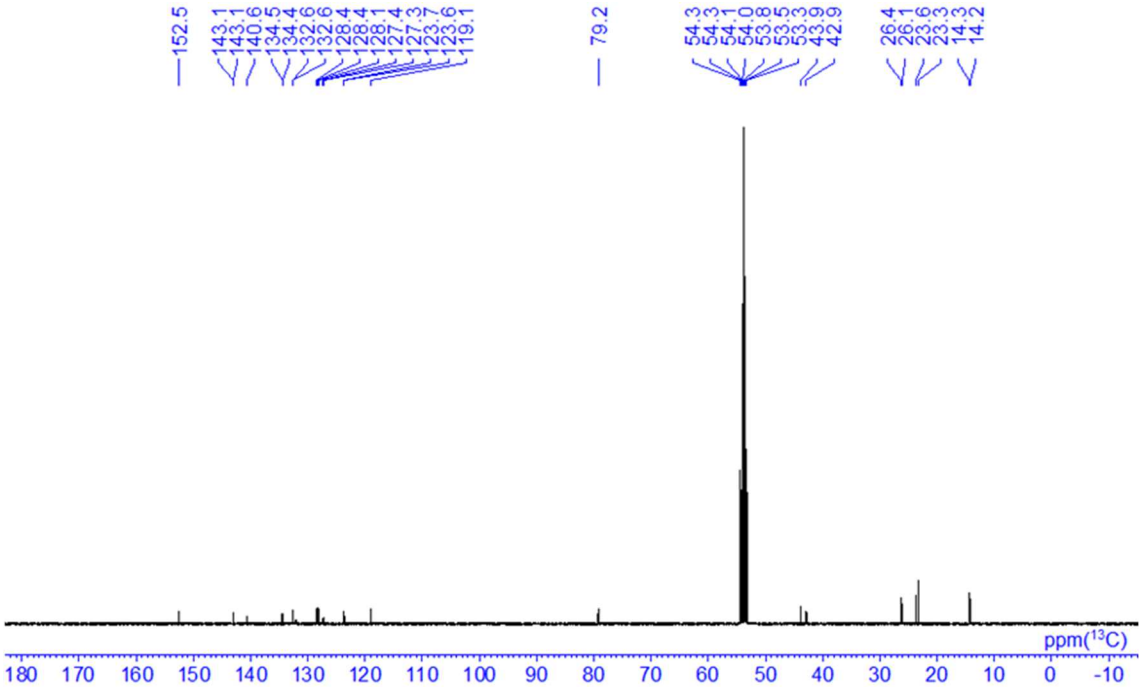

Chart 17. ^{13}C NMR spectrum of ***anti*-B2n** in CD_2Cl_2.

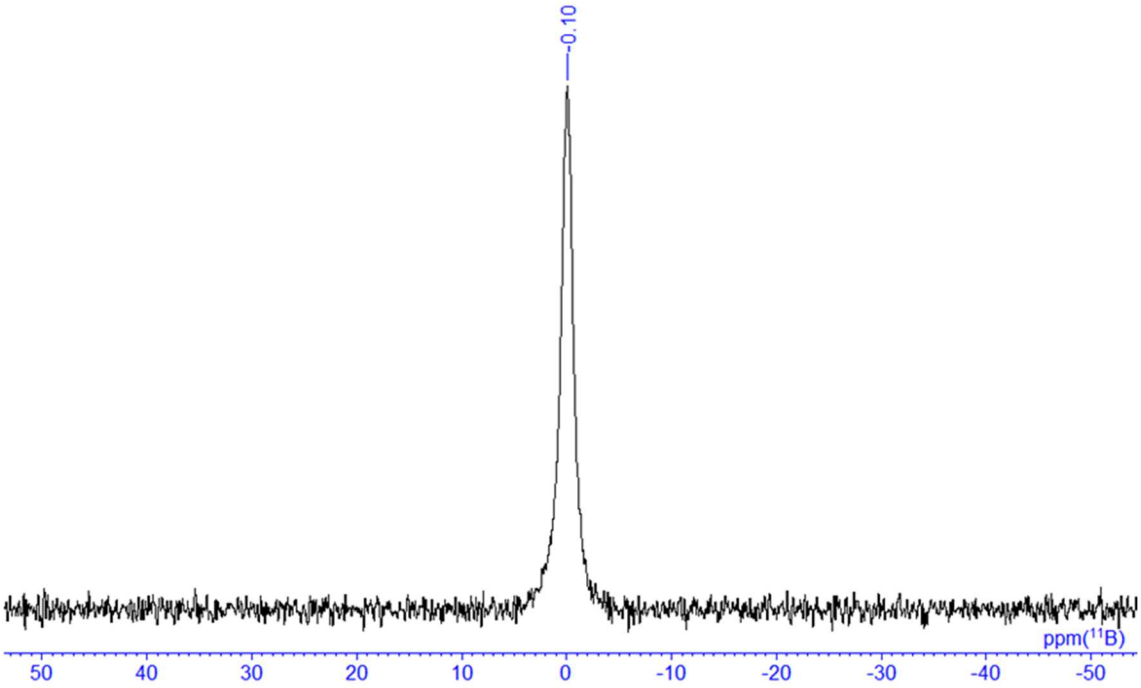

Chart 18. ^{11}B NMR spectrum of ***anti*-B2n** in CD_2Cl_2.

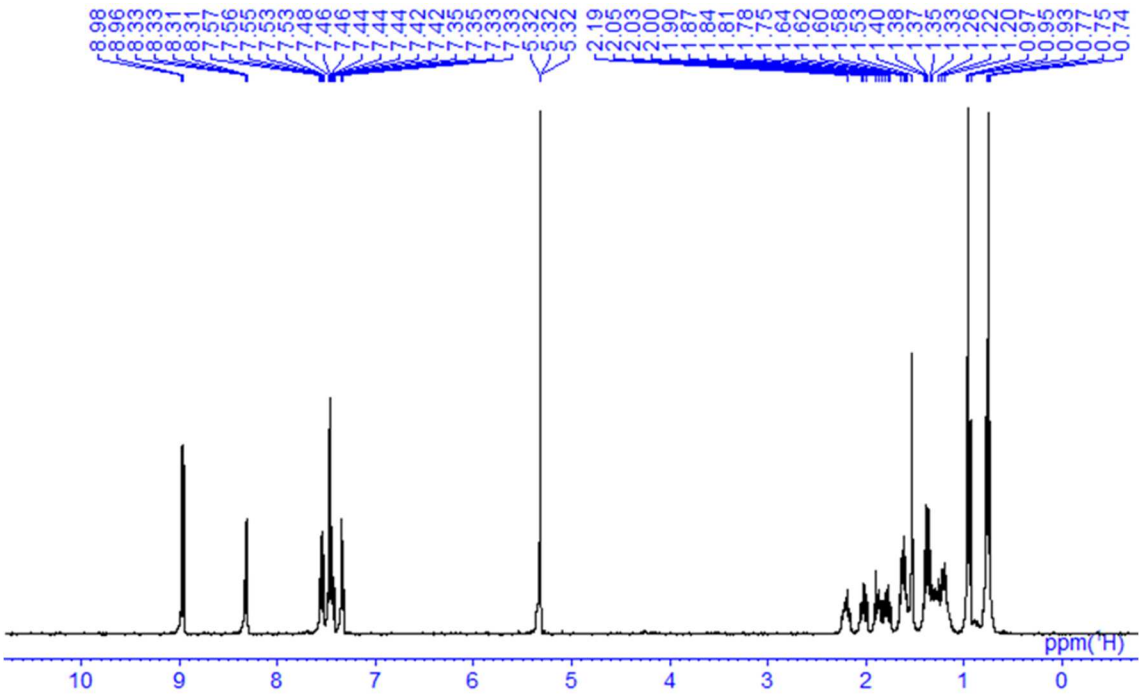

Chart 19. ^{1}H NMR spectrum of ***syn*-B2n** in CD_2Cl_2.

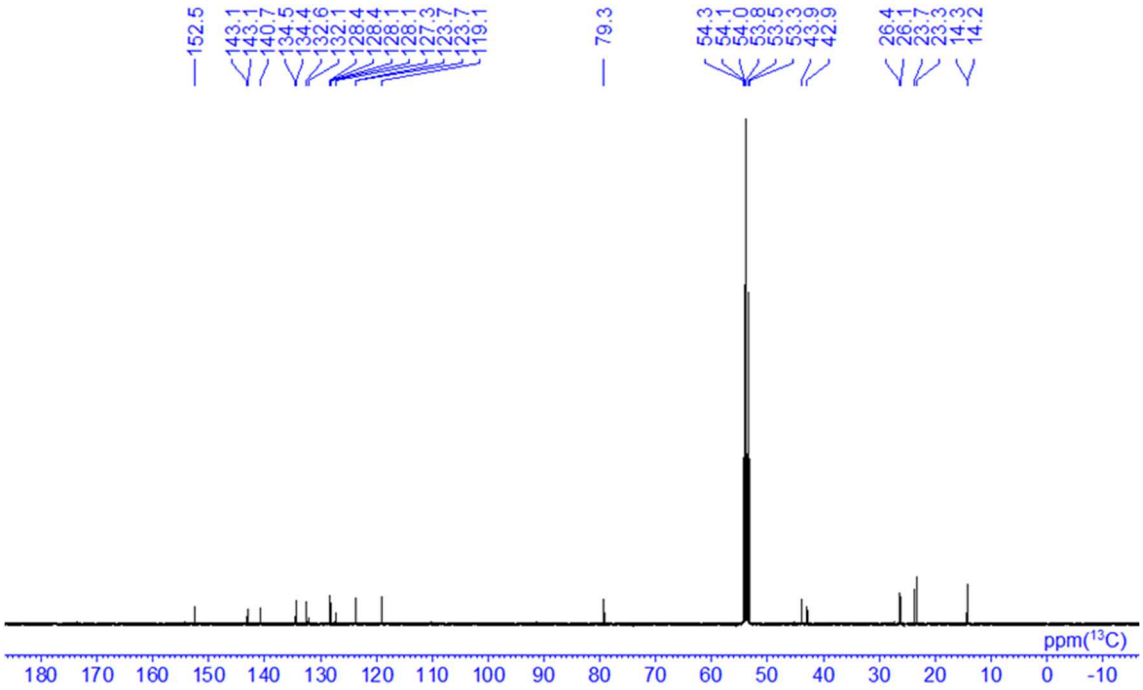

Chart 20. ^{13}C NMR spectrum of ***syn*-B2n** in CD_2Cl_2.

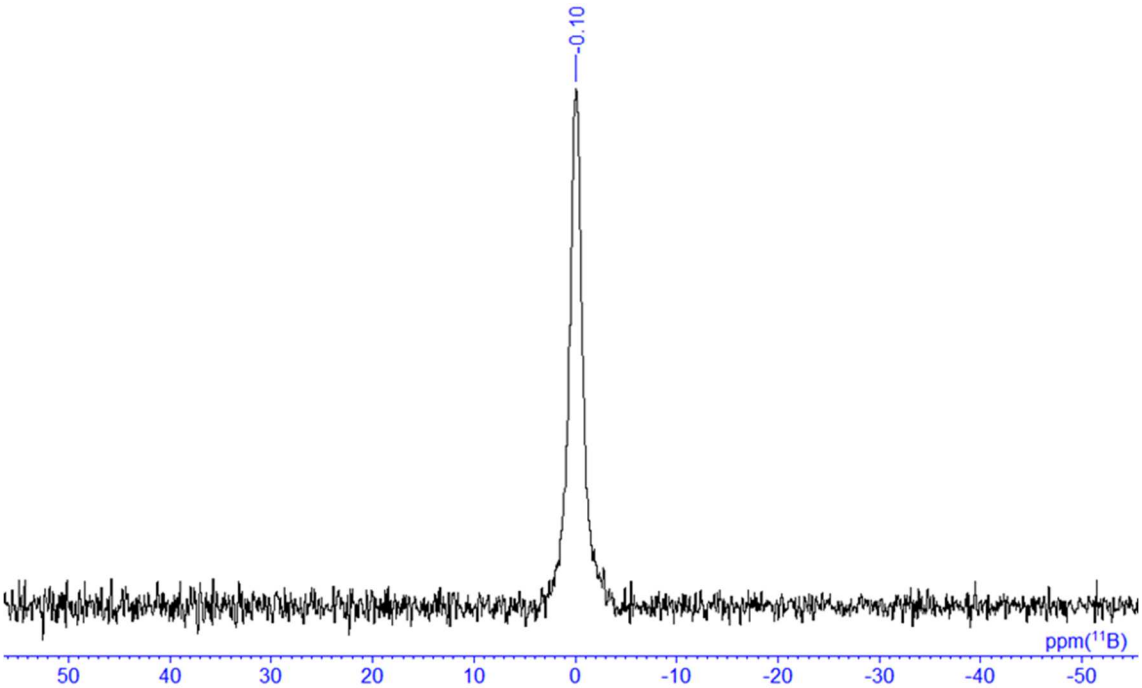

Chart 21. ^{11}B NMR spectrum of ***syn*-B2n** in CD_2Cl_2.

Single crystal X-ray structure analysis of B1

Intensity data were collected on a Rigaku R-AXIS RAPID imaging plate area detector with graphite monochromated MoKα radiation (λ = 0.71069 Å). The structures were solved and refined by full-matrix least-squares procedures based on F^2 (SHELXL-2014/7).[8]

Table S1. Crystallographic data of **B1**

Empirical formula	$C_{25}H_{28}BFN_2O_2$	
Formula weight	418.30	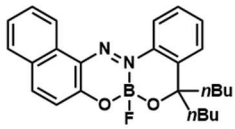
Temperature (K)	143(2)	
Wavelength (Å)	0.71075	
Crystal system, space group	Monoclinic, $P\ 2_1/n$	
Unit cell dimensions	a=8.670(3)	**B1**
	b=22.286(7)	CCDC # 2095545
	c=11.500(4)	
	α=90	
	β=99.990(4)	
	γ=90	
Volume (Å^3)	2188.3(13)	
Z, calculated density (g cm^{-3})	4, 1.270	
Absorption coefficient	0.085	
F(000)	888	
Crystal size (mm)	0.160×0.130×0.80	
θ range for data collection	3.006-27.515	
Limiting indices	$-11\leq h\leq 9$, $-28\leq k\leq 28$, $-14\leq l\leq 14$	
Reflections collected (unique)	4995/3954 [R(int)=0.0406]	
Completeness to theta	0.994	
Max. and min. transmission	1.000, 0.872	
Goodness-of-fit on F^2	1.087	
Final R indices [$I > 2\sigma(I)$]^a	R_1 = 0.0511, wR_2 = 0.1118	
R indices (all data)	R_1 = 0.0687, wR_2 = 0.1211	

[a] $R_1 = \Sigma(|F_0| - |F_c|)/\Sigma|F_0|$. w$R_2 = [\Sigma w(F^2_0 - F^2_c)^2/\Sigma w(F^2_0)^2]^{1/2}$. w = $1/[\sigma^2(F^2_0) + [(ap)^2 + bp]]$, where $p = [\max(F^2_0,0) + F^2_c]/3$.

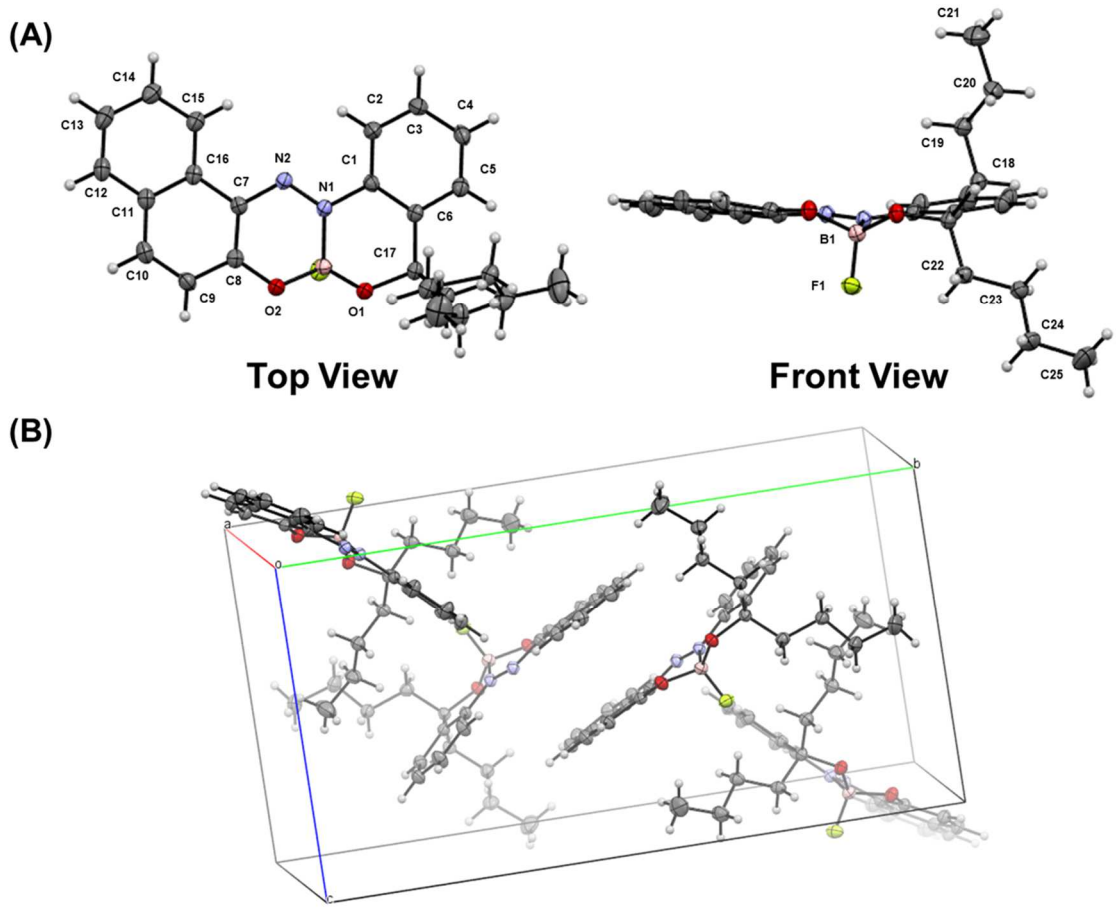

Figure S1. (A) ORTEP drawings and (B) packing diagrams of **B1**. Thermal ellipsoids are scaled to the 50% probability level.

Single crystal X-ray structure analysis of *anti*-B2n

Intensity data were collected on a Rigaku R-AXIS RAPID imaging plate area detector with graphite monochromated MoKα radiation (λ = 0.71069 Å). The structures were solved and refined by full-matrix least-squares procedures based on F^2 (SHELXL-2014/7)[8].

Table S2. Crystallographic data of ***anti*-B2n**

Empirical formula	$C_{40}H_{48}B_2F_2N_4O_4$	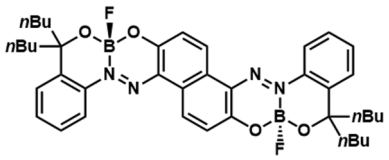
Formula weight	708.44	
Temperature (K)	143(2)	
Wavelength (Å)	0.71075	
Crystal system, space group	Monoclinic, $P\ 2_1/a$	
Unit cell dimensions	a=12.864(4)	***anti*-B2n**
	b=9.016(3)	CCDC # 2095548
	c=15.507(5)	
	α=90	
	β=95.242(4)	
	γ=90	
Volume (Å^3)	1791.0(10)	
Z, calculated density (g cm^{-3})	2, 1.314	
Absorption coefficient	0.091	
F(000)	752	
Crystal size (mm)	0.130×0.120×0.70	
θ range for data collection	3.124-27.488	
Limiting indices	$-16\leq h\leq 14$, $-11\leq k\leq 8$, $-20\leq l\leq 20$	
Reflections collected (unique)	4094/3022 [R(int)=0.0572]	
Completeness to theta	0.997	
Max. and min. transmission	1.000, 0.848	
Goodness-of-fit on F^2	1.118	
Final R indices [$I > 2\sigma(I)$]^a	R_1 = 0.0618, wR_2 = 0.1136	
R indices (all data)	R_1 = 0.0918, wR_2 = 0.1267	

[a] $R_1 = \Sigma(|F_0| - |F_c|)/\Sigma|F_0|$. w$R_2 = [\Sigma w(F^2_0 - F^2_c)^2/\Sigma w(F^2_0)^2]^{1/2}$. $w = 1/[\sigma^2(F^2_0) + [(ap)^2 + bp]]$, where $p = [\max(F^2_0,0) + F^2_c]/3$.

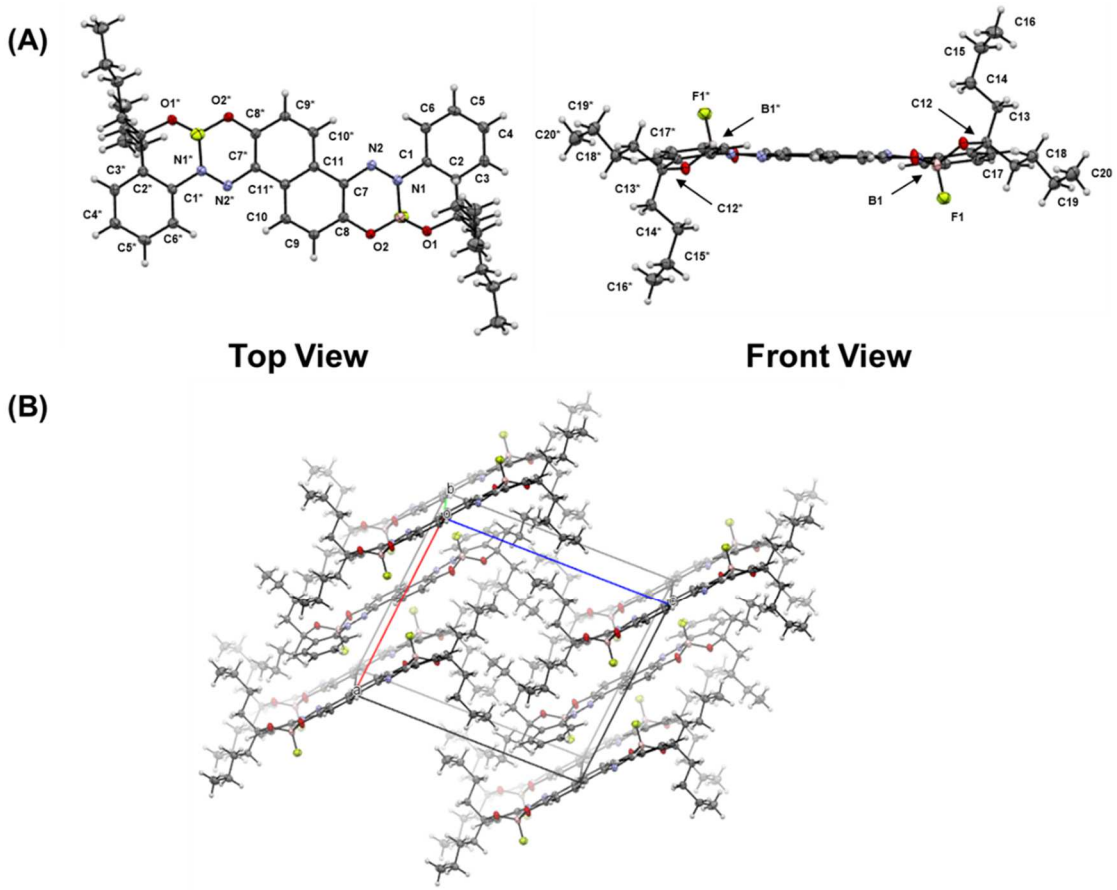

Figure S2. (A) ORTEP drawings and (B) packing diagrams of ***anti*-B2n**. Thermal ellipsoids are scaled to the 50% probability level.

Single crystal X-ray structure analysis of *anti*-B2b

Intensity data were collected on a Rigaku R-AXIS RAPID imaging plate area detector with graphite monochromated MoKα radiation (λ = 0.71069 Å). The structures were solved and refined by full-matrix least-squares procedures based on F^2 (SHELXL-2014/7)[8].

Table S3. Crystallographic data of ***anti*-B2b**

Empirical formula	$C_{44}H_{50}B_2F_2N_4O_4$	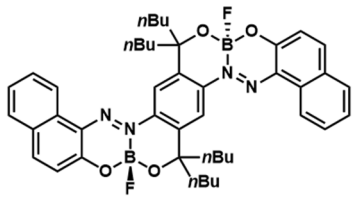
Formula weight	758.50	
Temperature (K)	143(2)	
Wavelength (Å)	0.71075	
Crystal system, space group	Monoclinic, $P\ 2_1/n$	
Unit cell dimensions	a=7.656(6)	
	b=21.051(15)	***anti*-B2b**
	c=12.118(9)	CCDC # 2095549
	α=90	
	β=96.077(11)	
	γ=90	
Volume (Å^3)	1942(3)	
Z, calculated density (g cm^{-3})	2, 1.297	
Absorption coefficient	0.089	
F(000)	804	
Crystal size (mm)	0.200×0.110×0.40	
θ range for data collection	3.162-27.48	
Limiting indices	$-9\leq h\leq 9$, $-21\leq k\leq 27$, $-15\leq l\leq 14$	
Reflections collected (unique)	4407/2145 [R(int)=0.1255]	
Completeness to theta	0.989	
Max. and min. transmission	0.996, 0.982	
Goodness-of-fit on F^2	0.905	
Final R indices [$I > 2\sigma(I)$]^a	R_1 = 0.0608, wR_2 = 0.0809	
R indices (all data)	R_1 = 0.1594, wR_2 = 0.0981	

[a] $R_1 = \Sigma(|F_0| - |F_c|)/\Sigma|F_0|$. w$R_2 = [\Sigma w(F^2_0 - F^2_c)^2/\Sigma w(F^2_0)^2]^{1/2}$. $w = 1/[\sigma^2(F^2_0) + [(ap)^2 + bp]]$, where $p = [\max(F^2_0,0) + F^2_c]/3$.

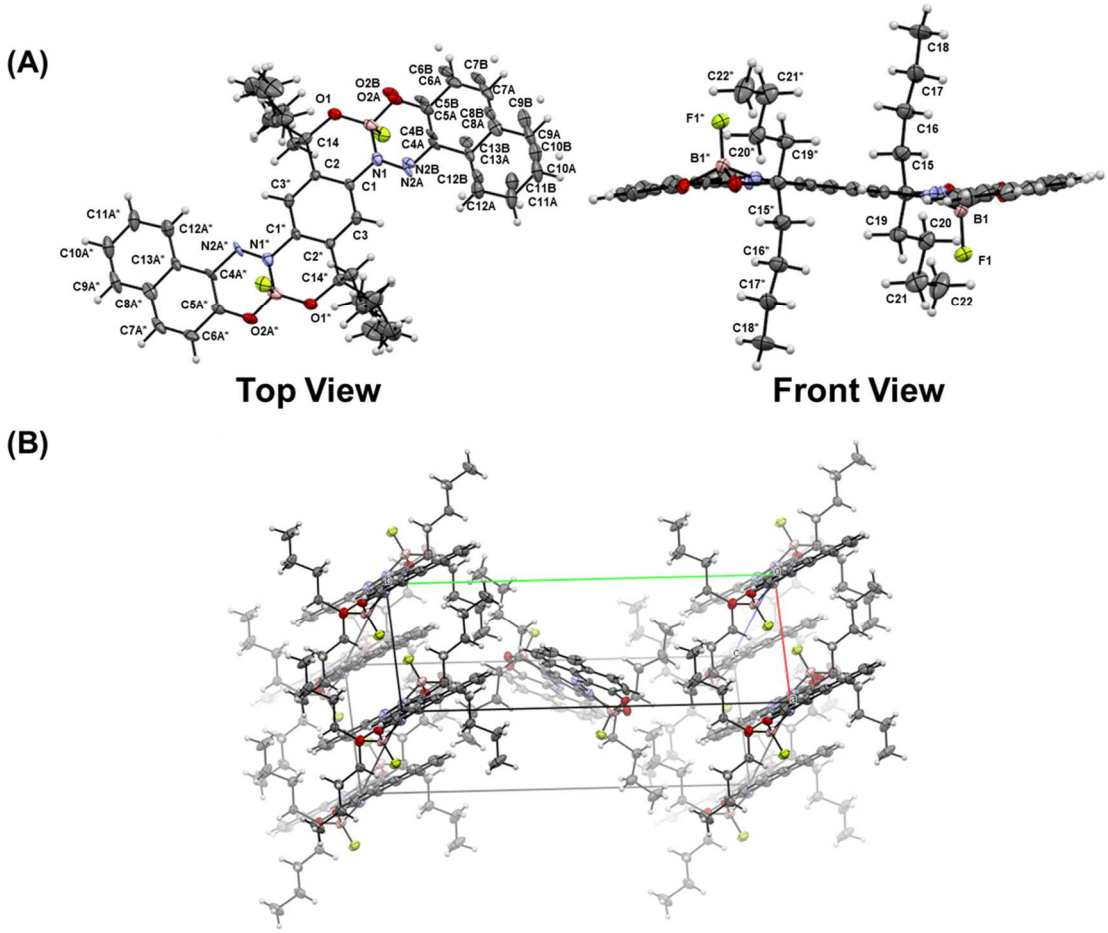

Figure S3. (A) ORTEP drawings and (B) packing diagrams of ***anti*-B2b**. Two components of the disorder were shown. The major component (part A) was shown with bonds. Thermal ellipsoids are scaled to the 50% probability level.

Absorption and PL properties

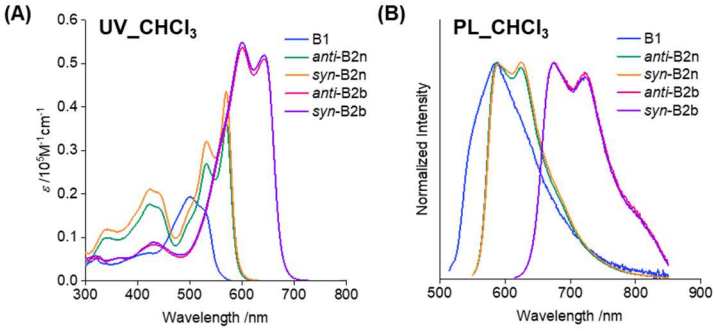

Figure S4. (A) UV–vis–NIR absorption and (B) PL spectra of **B1**, ***anti*-B2n**, ***syn*-B2n**, ***anti*-B2b**, and ***syn*-B2b** in $CHCl_3$ (1.0×10^{-5} M).

Table S4. Spectroscopic data of **B1**, ***anti*-B2n**, ***syn*-B2n**, ***anti*-B2b**, and ***syn*-B2b** in $CHCl_3$ (1.0×10^{-5} M).

	λ_{abs} /nm	λ_{PL} [a] /nm	ν [b]	Φ_{PL} [c]	τ [d] /ns	k_r [e] /10^8 s^{-1}	k_{nr} [e] /10^8 s^{-1}
B1	500, 524	589	2,100	< 0.01	–[f]	–[f]	–[f]
***anti*-B2n**	532, 570	588, 624	500	0.05	0.5	1.1	20
***syn*-B2n**	532, 570	590, 624	600	0.05	0.5	1.1	20
***anti*-B2b**	600, 642	674, 722	700	0.03	0.2	1.3	40
***syn*-B2b**	600, 642	675, 722	800	0.04	0.3	1.5	31

[a] Excited at $\lambda_{abs, min}$ (500 nm for **B1**, 532 nm for ***anti*-B2n** and ***syn*-B2n**, 600 nm for ***anti*-B2b**, and ***syn*-B2b**). [b] Stokes shift, $\nu = 1 / \lambda_{abs, max} - 1 / \lambda_{PL, min}$. [c] Absolute PL quantum yield, excited at $\lambda_{abs, min}$. [d] Emission lifetime, excited at 369 nm LED laser and monitored at $\lambda_{PL, min}$. [e] $k_r = \Phi_{PL} / \tau$, $k_{nr} = (1 - \Phi_{PL}) / \tau$. [f] Not detected.

Lippert–Mataga plots

The Lippert–Mataga plots were constructed (Figure S5) by using the relation below.

$$\nu = [2(\mu_e - \mu_g)^2/hca^3]\Delta f + \nu^o$$

$$\Delta f = [(\varepsilon - 1)/(2\varepsilon + 1)] - [(n^2 - 1)/(2n^2 + 1)]$$

ν : Stokes shift
ν^o : Stokes shift in the absence of solvent
μ_e: dipole moments in the ground state
μ_g: dipole moments in the excited state
a : Onsager cavity radius
Δf : orientation polarizability
ε : solvent dielectric constant
n : solvent refractive index

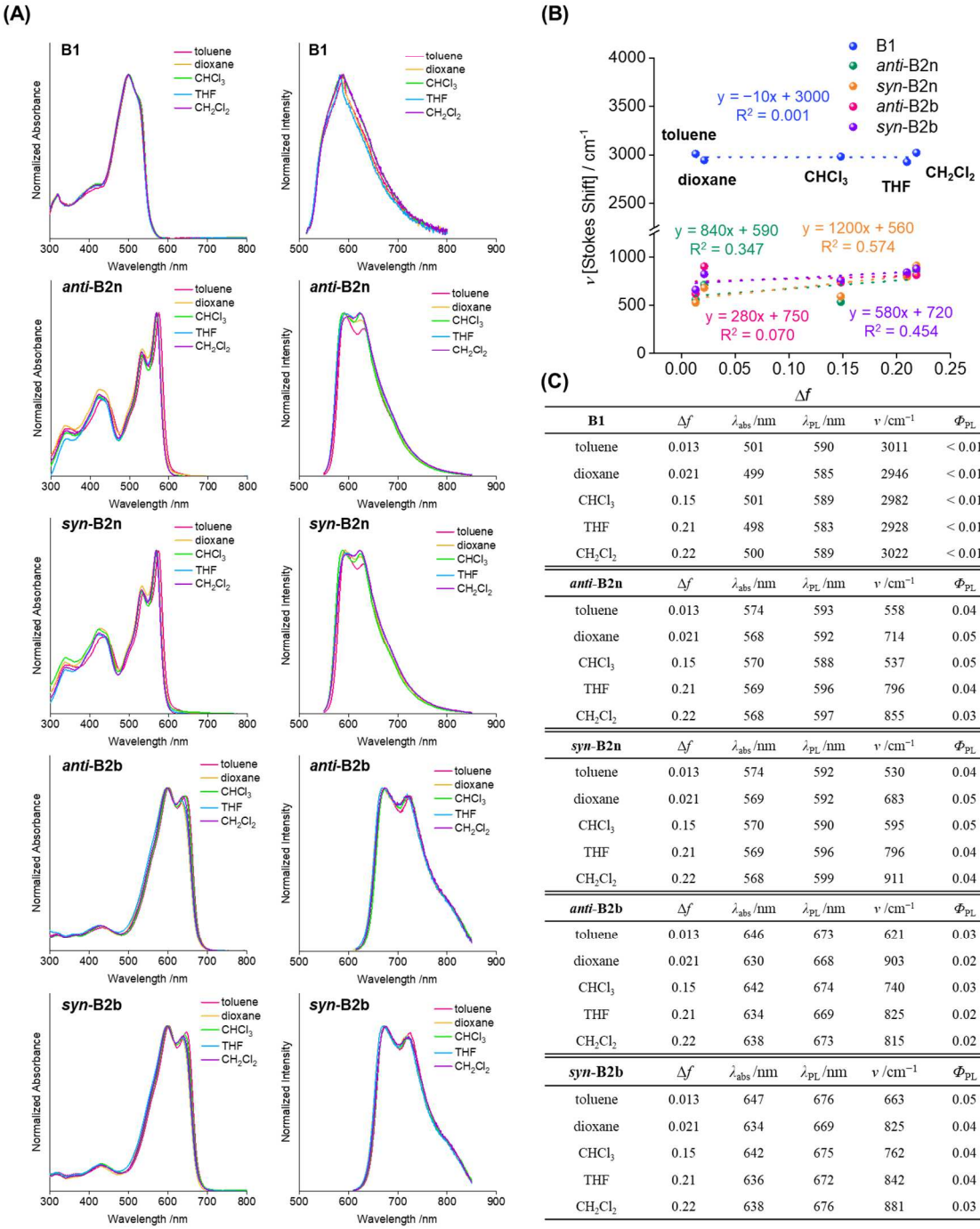

(C)

B1	Δf	λ_{abs} /nm	λ_{PL} /nm	ν /cm^{-1}	Φ_{PL}
toluene	0.013	501	590	3011	< 0.01
dioxane	0.021	499	585	2946	< 0.01
$CHCl_3$	0.15	501	589	2982	< 0.01
THF	0.21	498	583	2928	< 0.01
CH_2Cl_2	0.22	500	589	3022	< 0.01
***anti*-B2n**	Δf	λ_{abs} /nm	λ_{PL} /nm	ν /cm^{-1}	Φ_{PL}
toluene	0.013	574	593	558	0.04
dioxane	0.021	568	592	714	0.05
$CHCl_3$	0.15	570	588	537	0.05
THF	0.21	569	596	796	0.04
CH_2Cl_2	0.22	568	597	855	0.03
***syn*-B2n**	Δf	λ_{abs} /nm	λ_{PL} /nm	ν /cm^{-1}	Φ_{PL}
toluene	0.013	574	592	530	0.04
dioxane	0.021	569	592	683	0.05
$CHCl_3$	0.15	570	590	595	0.05
THF	0.21	569	596	796	0.04
CH_2Cl_2	0.22	568	599	911	0.04
***anti*-B2b**	Δf	λ_{abs} /nm	λ_{PL} /nm	ν /cm^{-1}	Φ_{PL}
toluene	0.013	646	673	621	0.03
dioxane	0.021	630	668	903	0.02
$CHCl_3$	0.15	642	674	740	0.03
THF	0.21	634	669	825	0.02
CH_2Cl_2	0.22	638	673	815	0.02
***syn*-B2b**	Δf	λ_{abs} /nm	λ_{PL} /nm	ν /cm^{-1}	Φ_{PL}
toluene	0.013	647	676	663	0.05
dioxane	0.021	634	669	825	0.04
$CHCl_3$	0.15	642	675	762	0.04
THF	0.21	636	672	842	0.04
CH_2Cl_2	0.22	638	676	881	0.03

Figure S5. (A) UV–vis–NIR absorption (left) and PL spectra (right), (B) Lippert–Mataga plots, and (C) spectroscopic data of **B1**, ***anti*-B2n**, ***syn*-B2n**, ***anti*-B2b**, and ***syn*-B2b** in the diluted solutions (1.0×10^{-5} M) at room temperature, excited at the wavelength of the absorption maximum of each compound.

Fluorescence in PMMA matrix

UV–vis absorption and PL measurement in polymer matrix were also carried out to evaluate the change in luminescence under conditions where molecular motion is suppressed. Each film was prepared by the following method: compound (1 wt%) and polymethyl methacrylate (PMMA) (typical M_w = 800,000, Nacalai tesque) were dissolved in chloroform (5.0×10^{-4} M for compound), and this solution was dropped onto a quartz plate (1 cm × 5 cm) and spin-coated (0.10 mL, 1000 rpm).

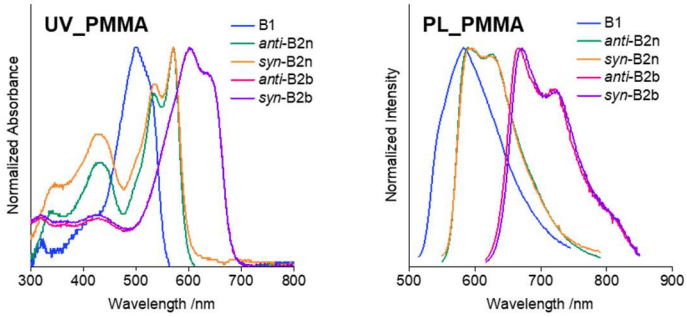

Figure S6. UV–vis–NIR absorption and PL spectra of **B1**, ***anti*-B2n**, ***syn*-B2n**, ***anti*-B2b**, and ***syn*-B2b** in 1 wt% PMMA dispersed film, excited at wavelengths of absorption maxima.

Table S5. Spectroscopic data of **B1**, ***anti*-B2n**, ***syn*-B2n**, ***anti*-B2b**, and ***syn*-B2b** in 1 wt% polymer dispersed film.

	λ_{abs} /nm	λ_{PL} [a] /nm	ν [b]	Φ_{PL} [c]	τ [d] /ns	k_r [e] /10^8 s^{-1}	k_{nr} [e] /10^8 s^{-1}
B1	501, 526	583	1,900	0.04	0.2 (74%) 1.5 (26%)	0.37	8.5
***anti*-B2n**	534, 570	589, 627	600	0.12	0.3 (44%) 1.6 (56%)	0.86	6.2
***syn*-B2n**	535, 570	591, 624	600	0.16	0.4 (28%) 2.0 (72%)	0.86	4.6
***anti*-B2b**	601, 636	667, 719	700	0.09	0.1 (83%) 0.7 (17%)	2.2	21
***syn*-B2b**	602, 636	672, 724	800	0.08	0.2 (64%) 0.6 (36%)	1.8	21

[a] Excited at $\lambda_{abs, min}$ (501 nm for **B1**, 534 nm for ***anti*-B2n**, 535 nm for ***syn*-B2n**, 601 nm for ***anti*-B2b**, and 602 nm for ***syn*-B2b**). [b] Stokes shift, $\nu = 1 / \lambda_{abs, max} - 1 / \lambda_{PL, min}$. [c] Absolute PL quantum yield, excited at $\lambda_{abs, min}$. [d] Emission lifetime, excited at 369 nm LED laser and monitored at $\lambda_{PL, min}$. [e] $k_r = \Phi_{PL} / \tau$, $k_{nr} = (1 - \Phi_{PL}) / \tau$. [b] Excited at $\lambda_{abs, min}$ of each condition. [c] Absolute PL quantum yield, excited at $\lambda_{abs, min}$.

PL lifetime decay curves

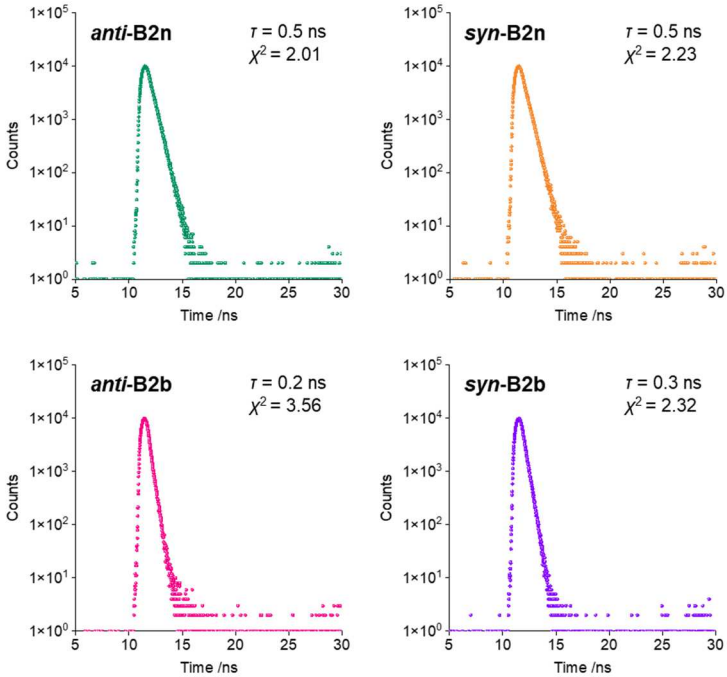

Figure S7. PL lifetime decay curves of **B1**, ***anti*-B2n**, ***syn*-B2n**, ***anti*-B2b**, and ***syn*-B2b** in $CHCl_3$ (1.0×10^{-5} M) at room temperature (excited at 369 nm with an LED laser). Their emissions at the PL peak tops were monitored.

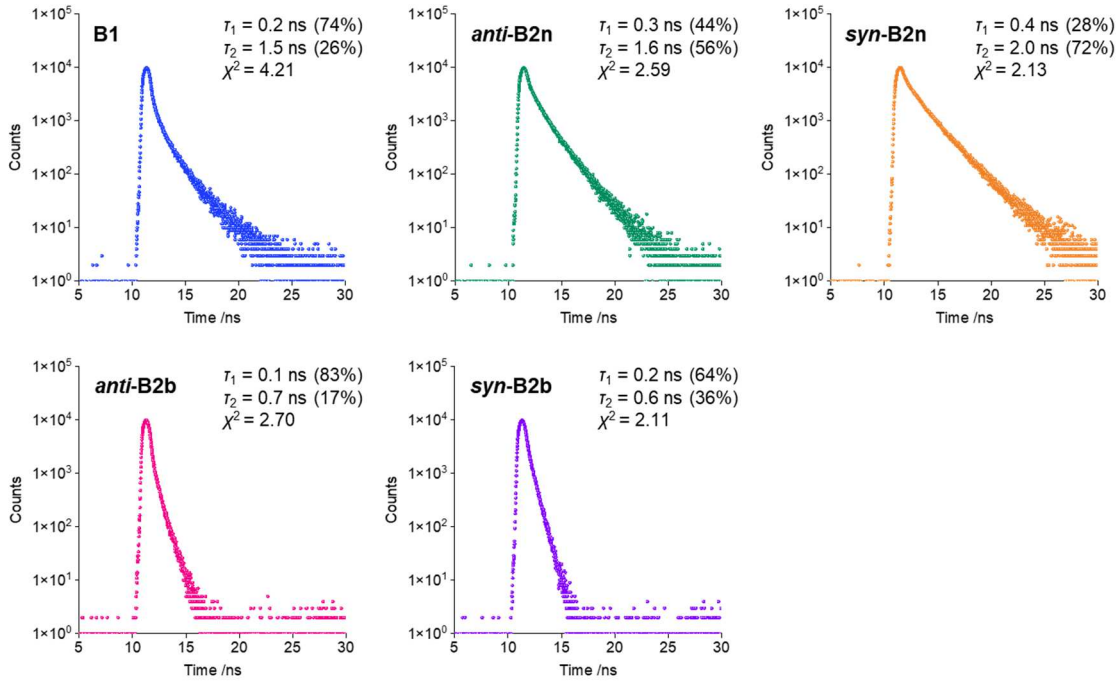

Figure S8. PL lifetime decay curves of **B1**, ***anti*-B2n**, ***syn*-B2n**, ***anti*-B2b**, and ***syn*-B2b** in 1 wt% PMMA dispersed film at room temperature (excited at 369 nm with an LED laser). Their emissions at the PL peak tops were monitored.

Variable temperature (VT) measurement

Variable temperature (VT) PL measurement was executed to investigate the inherent emissive potential of boron complexes and the effect of structural relaxation on luminescence in terms of solvent temperature. The measurement was carried out at 77 K first, then the temperature increased from 80 to 300 K in 5 K increments in 2-methyltetrahydrofuran (1.0×10^{-5} M). We checked the decrease in the intensity of **B1** more rapidly than bisboron complexes from around 100 K.

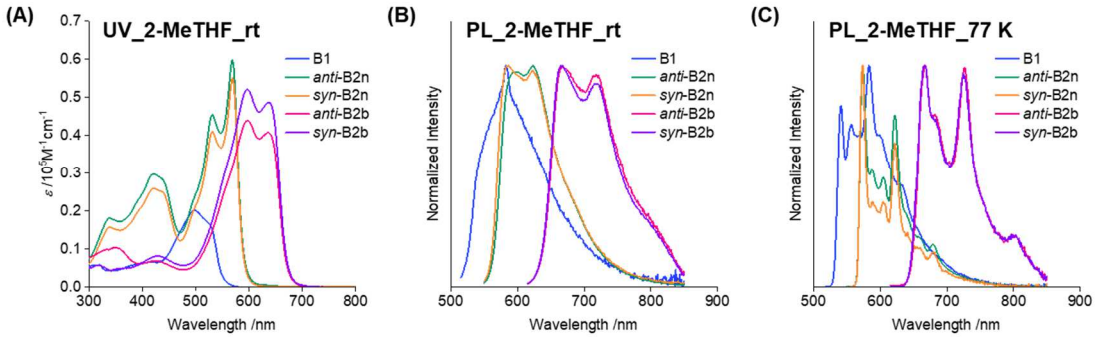

Figure S9. (A) UV–vis–NIR absorption at ambient temperature and PL spectra (B) at ambient temperature and (C) at 77 K of **B1**, ***anti*-B2n**, ***syn*-B2n**, ***anti*-B2b**, and ***syn*-B2b** in 2-methyltetrahydrofuran (1.0×10^{-5} M).

Table S6. Spectroscopic data of **B1**, ***anti*-B2n**, ***syn*-B2n**, ***anti*-B2b**, and ***syn*-B2b** in 2-methyltetrahydrofuran (1.0×10^{-5} M).

	At ambient temperature			At 77 K		
	λ_{abs} /nm	λ_{PL} [a] /nm	Φ_{PL} [b]	λ_{abs} /nm	λ_{PL} [a] /nm	Φ_{PL} [b]
B1	498	583	< 0.01	–	583	0.77
***anti*-B2n**	531, 569	597, 623	0.04	–	574, 622	0.68
***syn*-B2n**	531, 569	586, 623	0.04	–	574, 622	0.56
***anti*-B2b**	597, 636	668, 728	0.02	–	668, 727	0.32
***syn*-B2b**	597, 637	668, 718	0.04	–	666, 725	0.32

[a] Excited at $\lambda_{abs,\,min}$ (498 nm for **B1**, 531 nm for ***anti*-B2n** and ***syn*-B2n**, 597 nm for ***anti*-B2b** and ***syn*-B2b**).
[b] Absolute PL quantum yield, excited at $\lambda_{abs,\,min}$.

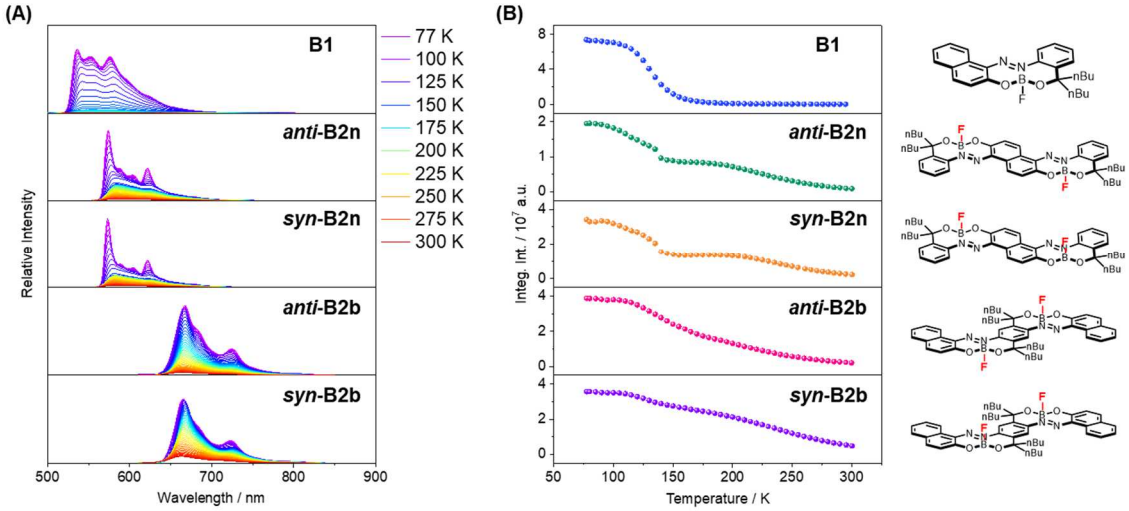

Figure S10. (A) VT PL spectra and (B) integral PL intensity versus temperature plots of **B1**, ***anti*-B2n**, ***syn*-B2n**, ***anti*-B2b**, and ***syn*-B2b** in 2-methyltetrahydrofuran (1.0×10^{-5} M) at the condition of 77 K and from 80 to 300 K in 5 K increments, excited at wavelengths of absorption maxima.

Variable viscosity (VV) measurement

Variable viscosity (VV) UV–vis absorption and PL measurement were performed to confirm the contribution of structural relaxation to emission properties in terms of solvent viscosity. Each solution was prepared by diluting chloroform solution (1.0×10^{-3} M) 100 times with four (highly viscous) solvents, a mixture of hexane and liquid paraffin (LP) in each ratio (hexane : LP = 100 : 0, 60 : 40, 20 : 80, 0 : 100) We observed increase in PL intensity of all compounds as an increase in solvent viscosity.

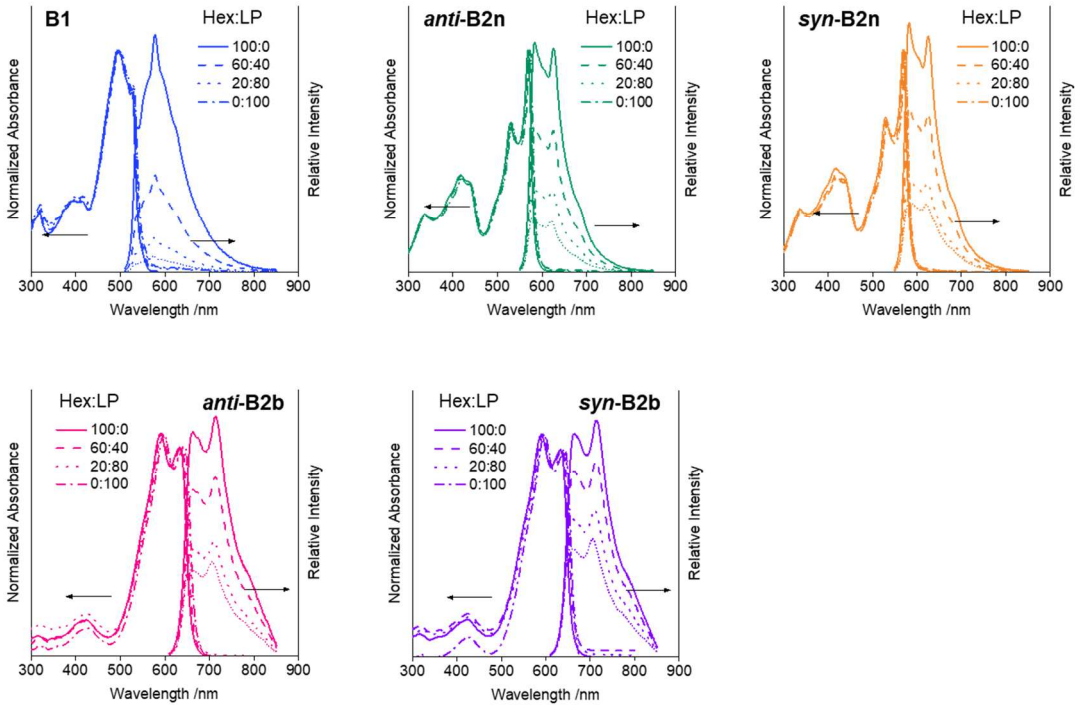

Figure S11. VV UV–vis absorption and PL spectra of **B1**, ***anti*-B2n**, ***syn*-B2n**, ***anti*-B2b**, and ***syn*-B2b** in a mixed solution of hexane and LP/$CHCl_3$ (99/1, v/v) (1.0×10^{-5} M), excited at wavelengths of absorption maxima.

Table S7. Spectroscopic data of **B1**, ***anti*-B2n**, ***syn*-B2n**, ***anti*-B2b**, and ***syn*-B2b** in a mixed solution of hexane and LP/$CHCl_3$ (99/1, v/v) (1.0×10^{-5} M).

	Hex : liquid paraffin	λ_{abs}/nm	λ_{PL} [a] /nm	Φ_{PL} [b]
B1	**100 : 0**	493, 526	575	< 0.01
	60 : 40	494, 528	577	< 0.01
	20 : 80	496, 530	578	< 0.01
	0 : 100	496, 530	578	0.01
***anti*-B2n**	**100 : 0**	529, 569	578, 620	0.03
	60 : 40	531, 571	581, 624	0.05
	20 : 80	532, 572	583, 626	0.10
	0 : 100	533, 573	584, 626	0.17
***syn*-B2n**	**100 : 0**	529, 568	586, 621	0.04
	60 : 40	531, 571	583, 623	0.06
	20 : 80	532, 572	582, 625	0.12
	0 : 100	533, 573	583, 625	0.20
***anti*-B2b**	**100 : 0**	590, 633	657, 705	0.02
	60 : 40	593, 637	659, 709	0.03
	20 : 80	596, 641	663, 713	0.06
	0 : 100	598, 643	663, 714	0.08
***syn*-B2b**	**100 : 0**	590, 633	657, 703	0.03
	60 : 40	593, 637	660, 708	0.05
	20 : 80	595, 640	662, 714	0.08
	0 : 100	597, 642	664, 712	0.11

[a] Excited at $\lambda_{abs,\ min}$ of each condition. [b] Absolute PL quantum yield, excited at $\lambda_{abs,\ min}$.

Fluorescence in aggregation and crystalline state

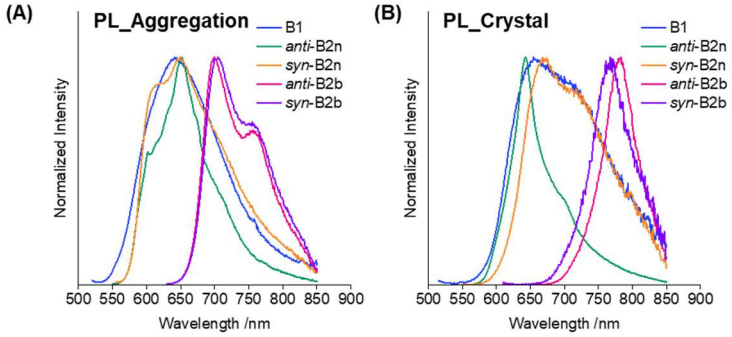

Figure S12. PL spectra of **B1**, ***anti*-B2n**, ***syn*-B2n**, ***anti*-B2b**, and ***syn*-B2b** (A) in THF/H_2O = 1/99 v/v (1.0×10^{-5} M) for preparing aggregates and (B) in crystalline state.

Transient Absorption Spectroscopy

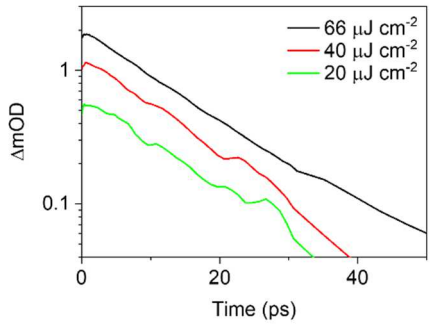

Figure S13. Transient absorption profiles of singlet excited states of **B1** in $CHCl_3$ (1.0×10^{-3} M) measured at 610 nm and in time ranges of 0–50 ps. The excitation intensity ranged from 20 to 66 μJ cm^{-2}. The excitation wavelength was 400 nm.

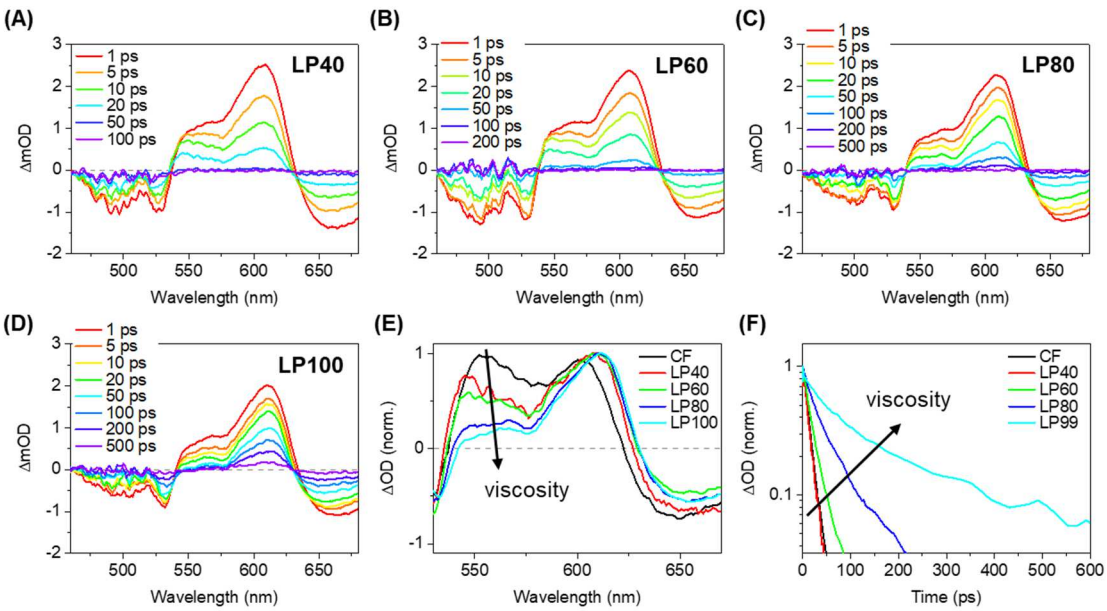

Figure S14. TA spectra of **B1** in a mixed solution of hexane and LP/$CHCl_3$ (99/1, v/v) (1.0×10^{-3} M) measured in time ranges of (A) 1–100 ps for LP40, (B) 1–200 ps for LP60, (C) 1–500 ps for LP80, and (D) 1–500 ps for LP100; *x* of LP*x* is LP fraction (vol%). (E) Normalized TA spectra of **B1** in $CHCl_3$ and various LP*x* solutions measured at 20 ps after photoexcitation, normalized to ΔOD values at 610 nm. (F) Transient absorption profiles of singlet excited states of **B1** in $CHCl_3$ and various LP*x* solutions. The excitation wavelength and intensity were 400 nm and 66 μJ cm^{-2}, respectively.

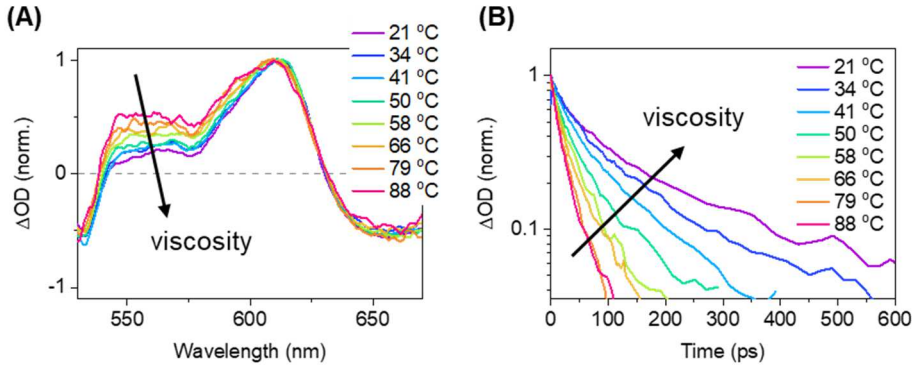

Figure S15. (A) Normalized VT TA spectra of **B1** in LP100 solution measured at 20 ps after photoexcitation and in temperature ranges of 21–88 °C, normalized to ΔOD values at 610 nm. (B) Transient absorption profiles of singlet excited states of **B1** in LP100 solution in temperature ranges of 21–88 °C. The excitation wavelength and intensity were 400 nm and 66 μJ cm^{-2}, respectively.

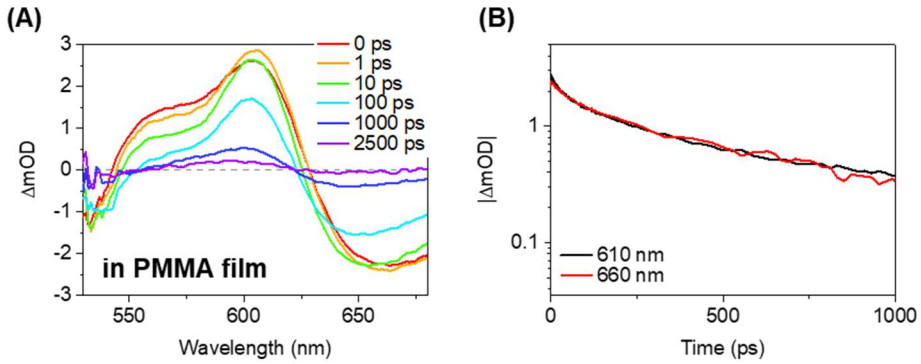

Figure S16. (A) TA spectra of **B1** in 1 wt% PMMA dispersed film measured in time ranges of 0–2500 ps. (B) Transient absorption profiles of singlet excited states and stimulated emission of **B1** in 1 wt% PMMA dispersed film measured at 610 nm and 660 nm, respectively. The excitation wavelength and intensity were 400 nm and 66 μJ cm^{-2}, respectively.

Table S8. Decay data of **B1**, ***anti*-B2n**, ***syn*-B2n**, ***anti*-B2b**, and ***syn*-B2b**.

Sample	Condition	λ_{obs} /nm (state)	Lifetime [a] /ps	τ_1 /ps (%)	τ_2 /ps (%)	τ_3 /ps (%)
B1 [b]	Chloroform	480 (GSB)	26			
	Chloroform	570 (S_1)	19			
	Chloroform	610 (S_1)	13			
	LP40	610 (S_1)	12			
	LP60	610 (S_1)	20	11 (54)	31 (46)	
	LP80	610 (S_1)	45	15 (39)	64 (61)	
	LP100 at 21 °C	610 (S_1)	151	51 (43)	264 (49)	
	LP100 at 34 °C	610 (S_1)	100	28 (50)	171 (50)	
	LP100 at 41 °C	610 (S_1)	75	23 (49)	125 (51)	
	LP100 at 50 °C	610 (S_1)	49	10 (36)	67 (64)	
	LP100 at 58 °C	610 (S_1)	37	11 (42)	56 (58)	
	LP100 at 66 °C	610 (S_1)	33	12 (51)	56 (49)	
	LP100 at 79 °C	610 (S_1)	23	7 (38)	33 (62)	
	LP100 at 88 °C	610 (S_1)	21	8 (50)	35 (50)	
	1 wt% PMMA dispersed film	610 (S_1)	553	31 (34)	282 (46)	2077 (20)
***anti*-B2n** [c]	Chloroform	570 (GSB)	450			
***mix*-B2b** [c]	Chloroform	650 (GSB)	210			

[a] Estimated by the transient absorption spectroscopy, monitored at λ_{obs}. [b] The excitation wavelength and intensity were 400 nm and 66 μJ cm^{-2}, respectively. [c] The excitation wavelength and intensity were 400 nm and 75 μJ cm^{-2}, respectively.

Cyclic voltammograms

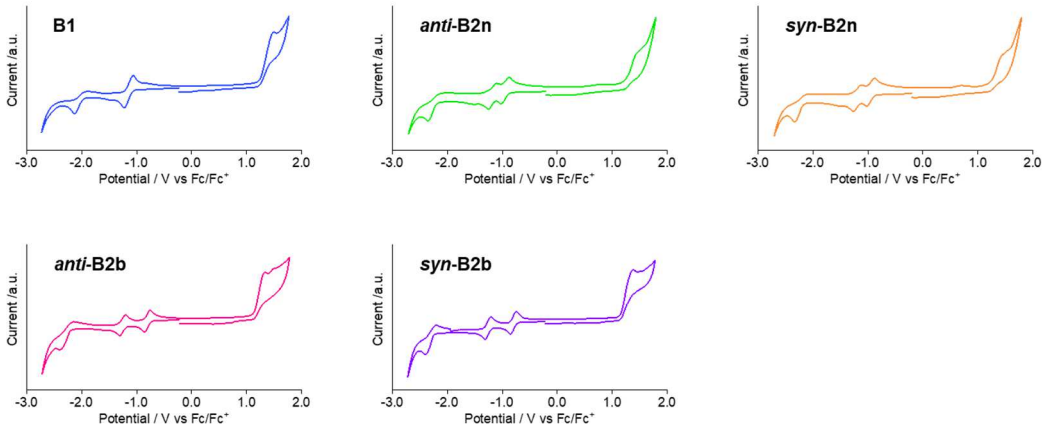

Figure S17. Cyclic voltammograms of **B1**, ***anti*-B2n**, ***syn*-B2n**, ***anti*-B2b**, and ***syn*-B2b** in CH_2Cl_2 (1.0×10^{-3} M) containing NBu_4PF_6 (0.10 M) using a glassy carbon (GC) working electrode, a Pt wire counter electrode, an Ag/AgCl reference electrode, and a Fc/Fc^+ external standard at room temperature with a scan rate of 0.1 V s^{-1}.

Table S9. Electrochemical data of **B1**, ***anti*-B2n**, ***syn*-B2n**, ***anti*-B2b**, and ***syn*-B2b**.

	E_{onset}^{red} / V	E_{onset}^{ox} / V	E_{LUMO} [a] / eV	E_{HOMO} [a] / eV
B1	−1.08	1.25	−3.72	−6.05
***anti*-B2n**	−0.88	1.24	−3.92	−6.04
***syn*-B2n**	−0.88	1.24	−3.92	−6.04
***anti*-B2b**	−0.74	1.14	−4.06	−5.94
***syn*-B2b**	−0.73	1.15	−4.07	−5.95

In CH_2Cl_2 (1.0×10^{-3} M) containing NBu_4PF_6 (0.10 M) using a glassy carbon (GC) working electrode, a Pt wire counter electrode, an Ag/AgCl reference electrode, and a Fc/Fc^+ external standard at room temperature with a scan rate of 0.1 V s^{-1}. [a] $E_{LUMO} = -4.8 - E_{onset}^{red}$, $E_{HOMO} = -4.8 - E_{onset}^{ox}$.[9,10]

Computational details for theoretical calculation

The Gaussian 16 program package[11] was used for computation. We optimized the geometries of the **B1'**, ***anti*-B2n'**, ***syn*-B2n'**, ***anti*-B2b'**, and ***syn*-B2b'** in the ground S_0 states and excited S_1 states, and calculated their molecular orbitals. The density functional theory (DFT) and time-dependent (TD) DFT were applied for the optimization of the geometries in the S_0 states at B3LYP/6-311G(d,p) level, and in the S_1 states at B3LYP/6-31+G(d,p) level, respectively. We calculated the energy of the transitions with optimized geometries in the S_0 and S_1 states by time-dependent (TD) DFT at B3LYP/6-311+G(d,p) level. The structure of model compounds, **B1'**, ***anti*-B2n'**, ***syn*-B2n'**, ***anti*-B2b'**, and ***syn*-B2b'**, are shown below.

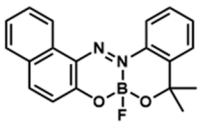

B1'

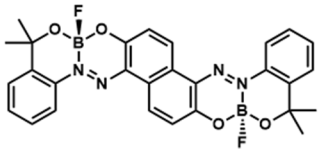

***anti*-B2n'**

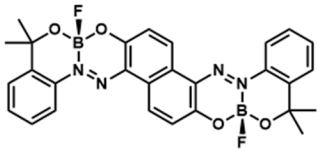

***syn*-B2n'**

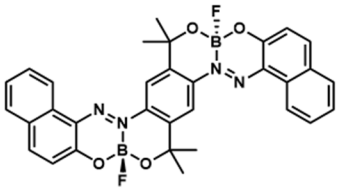

***anti*-B2b'**

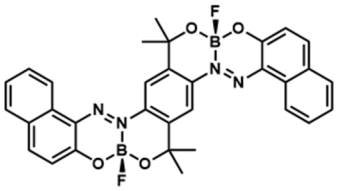

***syn*-B2b'**

Selected Kohn–Sham orbitals of model compounds

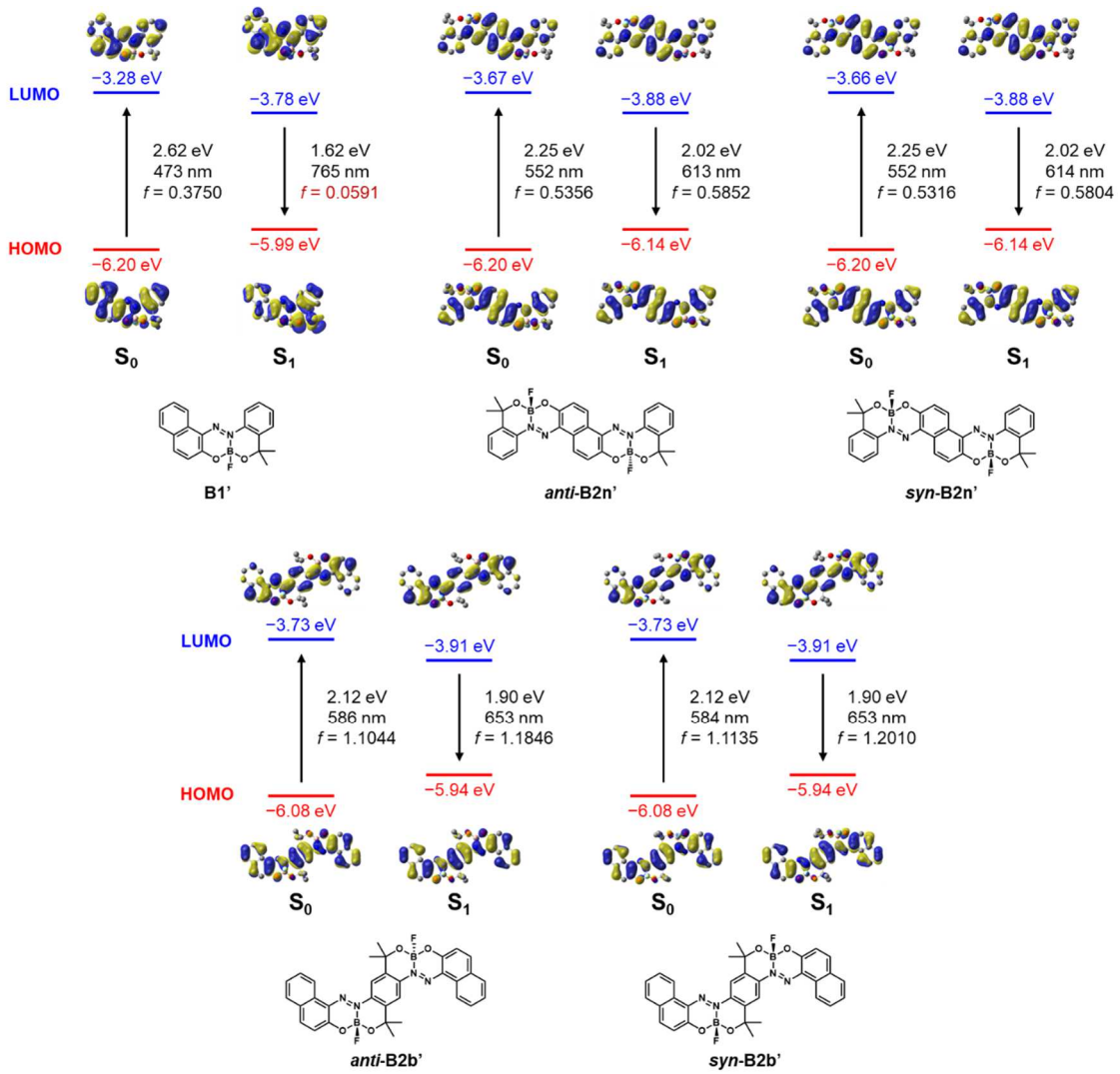

Figure S18. Selected Kohn–Sham orbitals of model compounds **B1'**, ***anti*-B2n'**, ***syn*-B2n'**, ***anti*-B2b'**, and ***syn*-B2b'** main transition band and contributed MOs with rate of contribution (*f*: oscillator strength) obtained with DFT or TD-DFT calculations (isovalue = 0.02). Hydrogens were omitted for clarity.

Optimized geometries in the ground and excited states

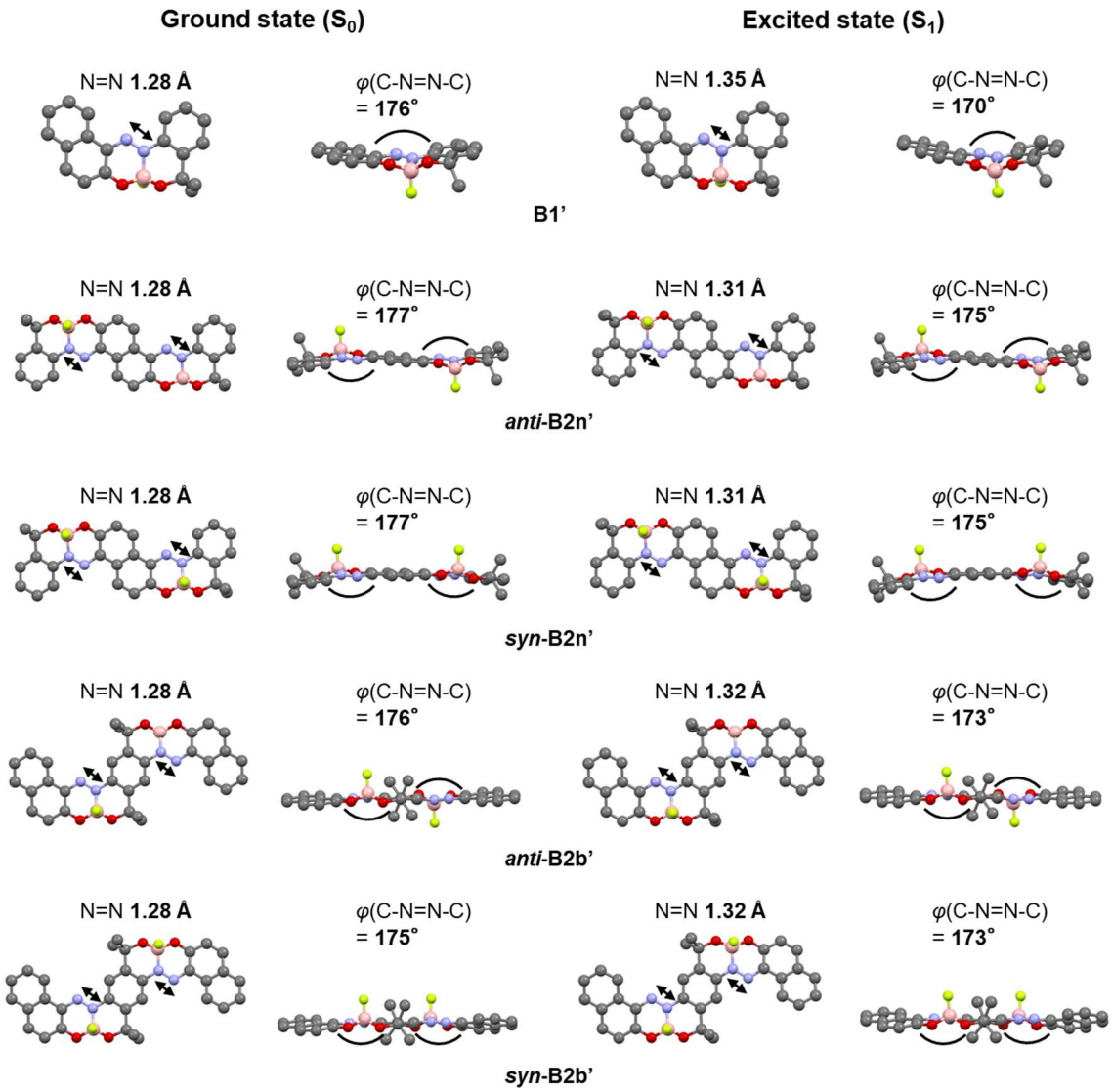

Figure S19. Optimized structures in the ground and excited states of **B1'**, ***anti*-B2n'**, ***syn*-B2n'**, ***anti*-B2b'**, and ***syn*-B2b'** obtained with DFT and TD-DFT calculations at the B3LYP/6-311G(d,p) and at the TD-B3LYP/6-311+G(d,p) levels, respectively. Hydrogens were omitted for clarity.

References

[1] T. Higashi, ABSCOR. Program for Absorption Correction.; Rigaku Corporation: Japan, **1995**.

[2] G. M. Sheldrick, SHELX-97. Programs for Crystal Structure Analysis.; University of Göttingen: Germany, **1997**.

[3] K. Wakita, Yadokari&XG. Program for Crystal Structure Analysis.; **2000**.

[4] L. J. Farrugia, *J. Appl. Cryst.* **1997**, *30*, 565

[5] A. B. Pangborn, M. A. Giardello, R. H. Grubbs, R. K. Rosen, F. J. Timmers, *Organometallics* **1996**, *15*, 1518–1520.

[6] D. Pletsch, F. da Silveira Santos, F. S. Rodembusch, V. Stefani, L. F. Campo, *New J. Chem.* **2012**, *36*, 2506–2513.

[7] J. Quinn, E. Jin, Y. Li, *Tetrahedron Lett.* **2015**, *56*, 2280–2282.

[8] G. M. Sheldrick, *Acta Cryst.* **2015**, *C71*, 3–8.

[9] J. Pommerehne, J.; Vestweber, H.; Guss, W.; Mahrt, R. F.; Bässler, H.; Porsch, M.; Daub, *Adv. Mater.* **1995**, *7*, 551–554.

[10] C. M. Cardona, W. Li, A. E. Kaifer, D. Stockdale, G. C. Bazan, *Adv. Mater.* **2011**, *23*, 2367–2371.

[11] Gaussian 16, Revision C.01, M. J. Frisch, G. W. Trucks, H. B. Schlegel, G. E. Scuseria, M. A. Robb, J. R. Cheeseman, G. Scalmani, V. Barone, G. A. Petersson, H. Nakatsuji, X. Li, M. Caricato, A. V. Marenich, J. Bloino, B. G. Janesko, R. Gomperts, B. Mennucci, H. P. Hratchian, J. V. Ortiz, A. F. Izmaylov, J. L. Sonnenberg, D. Williams-Young, F. Ding, F. Lipparini, F. Egidi, J. Goings, B. Peng, A. Petrone, T. Henderson, D. Ranasinghe, V. G. Zakrzewski, J. Gao, N. Rega, G. Zheng, W. Liang, M. Hada, M. Ehara, K. Toyota, R. Fukuda, J. Hasegawa, M. Ishida, T. Nakajima, Y. Honda, O. Kitao, H. Nakai, T. Vreven, K. Throssell, J. A. Montgomery, Jr., J. E. Peralta, F. Ogliaro, M. J. Bearpark, J. J. Heyd, E. N. Brothers, K. N. Kudin, V. N. Staroverov, T. A. Keith, R. Kobayashi, J. Normand, K. Raghavachari, A. P. Rendell, J. C. Burant, S. S. Iyengar, J. Tomasi, M. Cossi, J. M. Millam, M. Klene, C. Adamo, R. Cammi, J. W. Ochterski, R. L. Martin, K. Morokuma, O. Farkas, J. B. Foresman, and D. J. Fox, Gaussian, Inc., Wallingford CT, **2016**.